

The Dynamics of Shelf Forcing in Greenlandic Fjords

REBECCA H. JACKSON

Oregon State University, Corvallis, Oregon

STEVEN J. LENTZ

Woods Hole Oceanographic Institution, Woods Hole, Massachusetts

FIAMMA STRANEO

Scripps Institution of Oceanography, San Diego, California

(Manuscript received 21 March 2018, in final form 7 August 2018)

ABSTRACT


The fjords that connect Greenland's glaciers to the ocean are gateways for importing heat to melt ice and for exporting meltwater into the ocean. The transport of heat and meltwater can be modulated by various drivers of fjord circulation, including freshwater, local winds, and shelf variability. Shelf-forced flows (also known as the intermediary circulation) are the dominant mode of variability in two major fjords of east Greenland, but we lack a dynamical understanding of the fjord's response to shelf forcing. Building on observations from east Greenland, we use numerical simulations and analytical models to explore the dynamics of shelf-driven flows. For the parameter space of Greenlandic fjords, we find that the fjord's response is primarily a function of three nondimensional parameters: the fjord width over the deformation radius (W/R_d), the forcing time scale over the fjord adjustment time scale, and the forcing amplitude (shelf pycnocline displacements) over the upper-layer thickness. The shelf-forced flows in both the numerical simulations and the observations can largely be explained by a simple analytical model for Kelvin waves propagating around the fjord. For fjords with $W/R_d > 0.5$ (most Greenlandic fjords), 3D dynamics are integral to understanding shelf forcing—the fjord dynamics cannot be approximated with 2D models that neglect cross-fjord structure. The volume flux exchanged between the fjord and shelf increases for narrow fjords and peaks around the resonant forcing frequency, dropping off significantly at higher- and lower-frequency forcing.

1. Introduction

Fjords form a link between glaciers of the Greenland Ice Sheet and the ocean. They are the gateways for importing oceanic heat to melt ice and for exporting meltwater to the ocean. While submarine melting has been implicated as a driver of recent glacier acceleration (Holland et al. 2008; Nick et al. 2009; Joughin et al. 2012), little is known about the fjord-scale processes that modulate melt rates or transport meltwater (Straneo and Heimbach 2013). The submarine melt rate is expected to vary with the near-glacier velocity and ocean

temperature (Jenkins 2011), but basic questions about what drives temperature and velocity variability near Greenland's glaciers remain unanswered. Resolving the drivers of fjord circulation, fjord–shelf exchange, and fjord renewal is crucial for understanding how heat is imported to melt ice and how glacial meltwater is exported.

There are a variety of potential drivers of fjord circulation, including tides, local wind forcing, shelf variability, and freshwater inputs from rivers, submarine melting, or subglacial discharge [see fjord reviews in Farmer and Freeland (1983), Inall and Gillibrand (2010), Stigebrandt (2012), and Straneo and Cenedese (2015)]. Recent observational studies show that shelf-forced flows (from fluctuations in shelf density; also called the intermediary circulation) are the dominant mode of variability in two east Greenland fjords (Straneo et al. 2010; Jackson et al. 2014; Fraser and Inall 2018), consistent with studies of Scandinavian fjords that show shelf forcing to be the

 Denotes content that is immediately available upon publication as open access.

Corresponding author: Rebecca H. Jackson, rebecca.h.jackson@gmail.com

DOI: 10.1175/JPO-D-18-0057.1

© 2018 American Meteorological Society. For information regarding reuse of this content and general copyright information, consult the [AMS Copyright Policy](https://www.ametsoc.org/PUBSReuseLicenses) (www.ametsoc.org/PUBSReuseLicenses).

primary driver of fjord–shelf exchange in deep-silled fjords (e.g., [Pettersson 1920](#); [Stigebrandt 1981](#); [Arneborg 2004](#); [Inall et al. 2015](#)). Nevertheless, the underlying dynamics of these shelf-forced flows are largely unexplored, with no overarching dynamical framework for understanding shelf forcing across different fjords. Resolving the leading-order dynamics of shelf forcing is critical for assessing its importance (particularly in transporting heat and meltwater) relative to other modes of circulation and for accurate modeling of ocean–glacier interactions.

a. Background on shelf forcing in fjords

In general, the literature on shelf forcing in fjords is fragmentary and inconsistent, in both its terminology and underlying framework. The basic principle is that density variations outside a fjord can set up a pressure gradient between the fjord and shelf, driving baroclinic flows within the fjord. In this paper, we use the term “shelf forcing” to refer to baroclinic fjord flows that are driven by shelf density variations, but other common terms for this mechanism include “baroclinic pumping” or “intermediary circulation.” This last term arose from the finding that shelf forcing was largest in an intermediary layer between a surface brackish layer and the depth of a sill ([Stigebrandt 1990](#)). However, Greenlandic fjords often do not have a surface brackish layer (due to meltwater input at depth, as opposed to a river at the surface) nor a shallow sill with a deep isolated basin. Thus, the majority of the water column in many Greenlandic fjords might be subject to shelf forcing, not just an intermediary layer.

The role of shelf forcing has primarily been studied in Scandinavian fjords, many of which are short and narrow compared to the fjords of Greenland. [Pettersson \(1920\)](#) first documented that density fluctuations outside a fjord’s mouth drive a baroclinic response within the fjord, but it was not until the 1980s (e.g., [Svendsen 1980](#); [Klinck et al. 1981](#); [Holbrook et al. 1983](#)) that this baroclinic pumping was explored more extensively. Using a linear two-layer numerical model of a deep (500 m) fjord coupled to the shelf, [Klinck et al. \(1981\)](#) found that alongshore winds set up a boundary condition at the mouth of the fjord that drove a baroclinic circulation within the fjord. For example, during downwelling-favorable winds, the pycnocline would be depressed at the mouth while the sea surface would rise, driving inflow in the upper layer of the fjord and outflow in the lower layer. Expanding upon [Klinck et al.’s](#) work, [Stigebrandt \(1990\)](#) found that shelf forcing drove at least 10 times more exchange with the shelf than the estuarine circulation for a typical Norwegian fjord. Later studies by [Aure et al. \(1996\)](#) and [Arneborg \(2004\)](#) showed that high-frequency fluctuations were more efficient at driving exchange than low-frequency fluctuations.

There is limited discussion in most of the aforementioned papers about how pycnocline disturbances are communicated to the fjord. The exceptions are a few studies of particularly long and wide fjords that consider the propagation of density signals. [Proehl and Rattray \(1984\)](#) considered the wave response of the Strait of Juan de Fuca (typically classified as a fjord, despite its name) and found that disturbances from the mouth propagated up-basin as Kelvin waves. More recently, [Inall et al. \(2015\)](#) explored the propagation of coastal-trapped waves in a wide Arctic fjord in Svalbard.

The literature on shelf forcing in fjords is mostly site-specific, with no overarching framework or theory to predict the shelf-driven flow in different fjords or the magnitude of fjord–shelf exchange. There are two partial exceptions. First, [Stigebrandt and Aure \(1990\)](#) and [Aure et al. \(1996\)](#) derived an empirical relationship for the mean volume exchange between the fjord and shelf as a function of density variability on the shelf:

$$\bar{Q} = \beta \sqrt{HWA_f \frac{g\Delta M}{\rho_0}}, \quad (1)$$

where $\beta = 1.7 \times 10^{-5}$ is an empirical constant, H is the fjord mouth depth, W is the fjord mouth width, A_f is the surface area of the fjord, ρ_0 is the reference density, and ΔM (kg m^{-2}) is the standard deviation of the mass per unit area of the shelf water column from the mean sea surface down to sill depth. Although this equation lacks a solid dynamical framework and is empirically tuned to observations from Scandinavian fjords, it has seen a modest resurgence in recent fjord literature, being used by [Sutherland et al. \(2014\)](#) and [Inall et al. \(2015\)](#) and discussed in reviews by [Stigebrandt \(2010\)](#) and [Straneo and Cenedese \(2015\)](#).

An alternative, simpler expression for the volume flux driven by shelf forcing is referred to as the slab model ([Arneborg 2004](#); [Stigebrandt 2012](#)):

$$Q = -A_f \frac{\partial \eta}{\partial t}, \quad (2)$$

where Q is the upper-layer volume flux (equal and opposite to the lower-layer volume flux), A_f is the upstream surface area of the fjord, and η is the vertical displacement of the pycnocline. Equation (2) is a simple expression of volume conservation for a two-layer fjord, where it is assumed that the pycnocline heaving is uniform throughout the fjord (or it is valid more generally if used with the spatial average of η).

PARAMETER SPACE OF PREVIOUS STUDIES

To categorize the existing literature, two non-dimensional numbers can be used to form a 2D

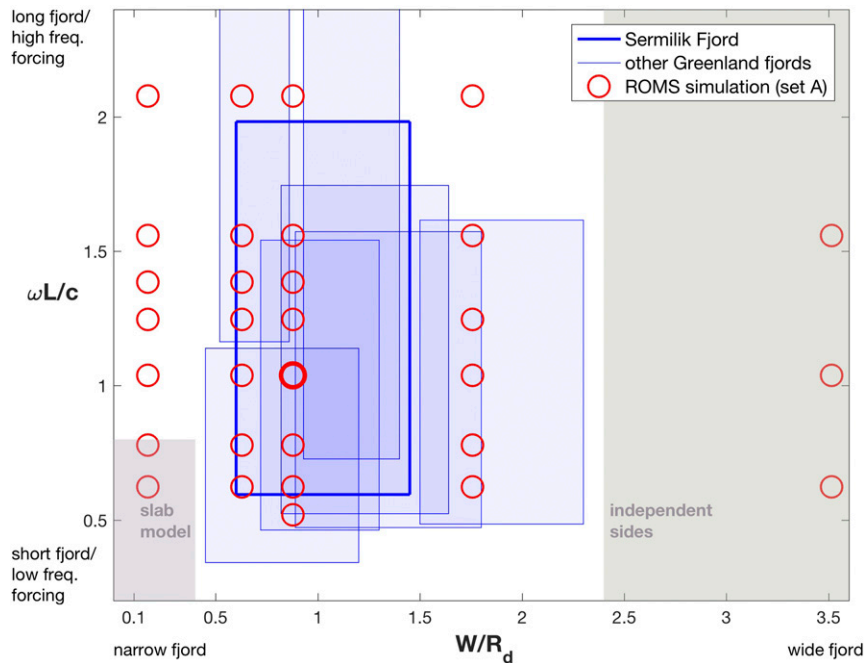


FIG. 1. Parameter space of $\omega L/c$ vs W/R_d . The slab model from Arneborg (2004) falls in the lower left corner, and very broad fjords with effectively independent sides (Inall et al. 2015; Proehl and Rattray 1984) fall on the far right of the domain. Eight Greenlandic fjords from Table 1 are shown in blue rectangles, with Sermilik Fjord in bold. ROMS simulations from set A are shown in circles, with the bold circle showing the control run to best approximate Sermilik conditions.

parameter space (Fig. 1): W/R_d , the fjord width divided by the deformation radius, and $\omega L/c$, the along-fjord adjustment time scale (L/c) divided by the forcing period ($1/\omega$), where $R_d = cf$ is the first-mode baroclinic deformation radius, c is the baroclinic phase speed, f is the Coriolis parameter, ω is the forcing frequency, and L is the fjord length. The ratio $\omega L/c$ can also be written as kL , that is, the ratio of the fjord length to the forcing wavelength, where $k = \omega/c$ is the wavenumber.

Most previous studies of Scandinavian fjords (e.g., Stigebrandt 1990; Arneborg 2004; Stigebrandt 2012) assume that the pycnocline heaves uniformly within the fjord, as in the slab model. This is based on two implicit assumptions. First, it is assumed that the response can propagate throughout the fjord on a time scale much shorter than that of the forcing fluctuations on the shelf, that is, $\omega L/c \ll 1$. This is a sound assumption in these short Scandinavian fjords [e.g., L is 28 km in Arneborg (2004) or 15 km in Stigebrandt (1990), with $c \approx 1 \text{ m s}^{-1}$ in both]. Second, these fjords are only a few kilometers wide, so they neglect rotational effects based on $W/R_d \ll 1$. Thus, these studies are situated in the lower left corner of the parameter space in Fig. 1.

The studies of Proehl and Rattray (1984) and Inall et al. (2015) fall on the opposite side of this parameter

space. They study the propagation of coastally trapped waves in large fjords, where the width is several times the deformation radius. The effects of rotation and wave propagation are paramount, but they only consider fjords that are wide enough for the sides to be effectively independent (Fig. 1). There remains a large portion of this parameter space that is unexplored, particularly the transition through $W/R_d \sim O(1)$.

b. The dynamics of shelf forcing in Greenland's fjords

Many fjords in Greenland fall in the unexplored region of parameter space where $W/R_d \sim O(1)$. Although several studies argue that Greenlandic fjords are narrow enough to model in 2D (e.g., Sciascia et al. 2014; Gladish and Holland 2015; Xu et al. 2012; Cowton et al. 2015), the high-latitude fjords of Greenland have widths on the same order as the deformation radius. The values of W/R_d for eight of the best-studied fjords in Greenland are shown in Table 1: all have median values of W/R_d between 0.7 and 2.0. These Greenlandic fjords are not clearly in the narrow limit of $W/R_d \ll 1$.

In terms of the along-fjord adjustment time scale, the fjords at the termini of Greenland's major glaciers are long enough that a baroclinic signal will take $O(1)$ day to

TABLE 1. Values of W/R_d and $\omega L/c$ for eight fjords in Greenland. For W/R_d , the median value is listed, followed by the minimum and maximum in brackets. This range is based on the variability in each fjord's width, assuming a constant value for c derived from the associated paper. To estimate $\omega L/c$, we assume a broad synoptic band forcing at periods of 3–10 days, with the central value corresponding to 6 days.

| Fjord | W/R_d | $\omega L/c$ | Source |
|-----------------------|----------------|----------------|-----------------------------|
| Sermilik Fjord | 0.8 [0.6, 1.5] | 1.0 [0.6, 2.0] | Sutherland et al. (2014) |
| Petermann Fjord | 2.0 [1.5, 2.3] | 0.8 [0.5, 1.6] | Johnson et al. (2011) |
| Kangerdlugssuaq Fjord | 1.0 [0.7, 1.3] | 0.8 [0.5, 1.5] | Inall et al. (2014) |
| Ilulissat Icefjord | 0.8 [0.5, 1.2] | 0.6 [0.3, 1.1] | Gladish and Holland (2015) |
| Rink Fjord | 1.1 [0.9, 1.8] | 0.8 [0.5, 1.6] | Bartholomaeus et al. (2016) |
| Store Fjord | 0.9 [0.8, 1.6] | 0.9 [0.5, 1.7] | Chauché et al. (2014) |
| Godthåbsfjord | 0.7 [0.5, 0.9] | 1.9 [1.2, 3.9] | Mortensen et al. (2011) |
| Kangerlussuup Sermia | 1.2 [0.9, 1.4] | 1.2 [0.7, 2.4] | Bartholomaeus et al. (2016) |

reach the head of the fjord (Table 1 and references therein)—shorter than the time scale of most synoptic wind forcing but not significantly. By assuming that fjords are subject to forcing in a broad synoptic time band (here defined as periods of 3–10 days), we can estimate $\omega L/c$ for each fjord in Table 1 and place these fjords in the parameter space of Fig. 1. Most of the Greenlandic fjords fall in the middle of Fig. 1, where the importance of cross-fjord structure and along-fjord propagation is not obvious.

Several recent studies have investigated the role of shelf forcing in Greenlandic fjords with 2D models (Gladish and Holland 2015; Sciascia et al. 2014) and 3D models (Cowton et al. 2016; Carroll et al. 2017; Fraser and Inall 2018). The extent to which Greenlandic fjords can be represented by 2D dynamics has not yet been fully addressed. Additionally, several of these studies (Gladish and Holland 2015; Sciascia et al. 2014; Cowton et al. 2016) impose shelf forcing through a boundary condition at the fjord mouth, rather than modeling the shelf region outside. In Sciascia et al. (2014), this model boundary condition mixes the upper and lower layer near the mouth, creating an intermediate-density water mass that propagates into the fjord as a gravity current. This is different than the mechanism suggested by observations in east Greenland fjords of heaving or waves on the pycnocline (a process that does not require any mixing). Accurate modeling of shelf forcing and exchange between the fjord and shelf likely requires including the shelf region outside the fjord in the model domain (Klinck et al. 1981). Carroll et al. (2017) and Fraser and Inall (2018) have made important steps in this regard by using 3D models of Greenlandic fjords and their adjacent shelves to examine the role of shelf forcing (along with other drivers of circulation).

While the aforementioned studies examine the impact of shelf forcing on fjord circulation and renewal, none of them explains the underlying dynamics of shelf-forced flows, how the fjord response will vary between different

fjords, or the relationship between the forcing signal and the fjord response. Shelf-forced flows might play an important role in fluxing heat, salt, and meltwater in certain fjords, but questions of tracer transport and renewal cannot be adequately answered without a fundamental framework for the dynamics of shelf-forced flows. In this paper, we investigate the role of shelf forcing in Greenlandic fjords, which occupy a part of parameter space that has been largely ignored. We attempt to address the following questions: What is the volume flux exchanged between fjord and shelf from shelf forcing? How does the fjord's response change with the forcing frequency, fjord geometry, and stratification? When can a fjord be approximated as two-dimensional and when does cross-fjord structure become important?

c. Motivating observations from east Greenland fjords

The modeling in this study is guided by observations from two east Greenland fjords, Sermilik and Kangerdlugssuaq, described in Jackson et al. (2014) and Jackson and Straneo (2016). Sermilik and Kangerdlugssuaq are deep-silled fjords (>500 m throughout) in a region where the shelf ocean is relatively wide (~150 km) and deep (~200 m). Troughs or canyons (>400 m deep) in the shelf extend from the fjord mouths to the shelf break.

In both fjords, shelf forcing dominates the variability in the velocity and density fields, and the most salient results from Jackson et al. (2014) and Jackson and Straneo (2016) are briefly reviewed here. In the moored records from Sermilik Fjord, the velocity is primarily a two-layer baroclinic flow with peak energy at 6-day periods. The fluctuating upper-layer velocities are typically $0.3\text{--}0.5\text{ m s}^{-1}$, occasionally exceeding 0.8 m s^{-1} , and they are associated with pycnocline heaving from tens of meters to one hundred meters in the vertical. On synoptic time scales of 3–10-day periods (subinertial and subtidal), the fjord flows are highly coherent with density fluctuations observed outside the fjord, on the shelf

just upstream of the fjord's mouth. Shelf density fluctuations, in turn, are primarily driven by regional alongshore winds (Harden et al. 2014). Comparison of mid- and inner-fjord moorings shows that, toward the head of the fjord, the velocity decays and the pycnocline fluctuations are mildly amplified.

These two fjords on the southeast coast of Greenland are in a region of exceptionally strong winds. On the shelf, low pressure storm systems compress against Greenland's steep topography and cause frequent, intense alongshore winds (Moore and Renfrew 2005). Additionally, the fjords are subject to less frequent but stronger down-fjord winds from the ice sheet (Oltmanns et al. 2014). The strongest of these wind events (~ 4 per year) drive significant exchange between the fjord and shelf (Spall et al. 2017), but shelf-forced flows are nearly continuous throughout the year and are the dominant mode of variability within the fjord.

In addition to wind and shelf forcing, Greenlandic fjords are also subject to buoyancy forcing from subglacial discharge, surface runoff, and submarine melting of glaciers and icebergs. During the summer months, a mean exchange flow is observed in Sermilik Fjord, with inflow at depth and outflow in a thick upper layer, which has been attributed to freshwater forcing (Jackson and Straneo 2016). The shelf forcing drives fluctuating velocities ($\sim 50 \text{ cm s}^{-1}$) that are much larger than the summer mean velocity ($\sim 4 \text{ cm s}^{-1}$), and the shelf-forced dynamics do not appear to be affected by the emergence of a mean flow in the summer. Thus, we focus here on the dynamics of shelf forcing and examine it in isolation of other forcings.

2. Methods

Based on the observations from Sermilik and Kangerdlugssuaq Fjords, we are interested in the propagation of density signals from the shelf that drive baroclinic fjord flows at subtidal and subinertial time scales. On a realistic shelf with both topography and stratification, coastal-trapped waves propagate density signals along the coast and represent a hybrid between barotropic shelf waves and internal Kelvin waves (Allen 1975; Huthnance 1978). The nondimensional slope Burger number is

$$S = \frac{\alpha N}{f}, \quad (3)$$

where α is the bottom slope, and N is the buoyancy frequency. When $S \gg 1$, coastal-trapped waves behave as pure internal Kelvin waves (e.g., Brink 1991). Around Sermilik Fjord, steep topography and strong stratification lead to large values of the slope Burger number:

$S = 23 \pm 6$ in the nonsummer and 45 ± 12 in the summer. Thus, subinertial pycnocline variability in this region should propagate with the properties of Kelvin waves. This is likely true for much of the coast around Greenland, where topography is generally steep and the water column is highly stratified. For this reason, we conduct idealized numerical simulations with vertical walls at the coast (i.e., in the limit of $\alpha \rightarrow \infty$ and thus $S \gg 1$) to examine the propagation of Kelvin waves on the shelf and through the fjord. We explore the response to shelf forcing across a range of fjord geometries and forcing frequencies using these simulations and two analytical models.

a. ROMS simulations of fjord and adjacent shelf

The response of a fjord to shelf forcing is simulated with an idealized configuration in the Regional Ocean Modeling System (ROMS; Shchepetkin and McWilliams 2005), a free-surface, hydrostatic, primitive equation model. In the model simulations, a rectangular fjord connects to an adjacent shelf region, with a flat bottom at 600-m depth and vertical walls between the ocean and land (Fig. 2a). The fjord geometry varies between different runs, while the shelf region remains constant at 310 km in the alongshore direction and 96 km in the cross-shore direction. The control run has fjord dimensions of $90 \text{ km} \times 7 \text{ km}$ to approximately match the geometry of Sermilik Fjord. The simulations use a stretched grid of resolution $\Delta x = \Delta y = 250 \text{ m}$ in the fjord and on the nearby shelf (within 150 km of the fjord mouth) that reduces to 1000-m horizontal resolution at the domain boundaries.

The model contains 30 levels of a stretched vertical grid, ranging from 7-m vertical resolution at the surface to 72 m at the bottom (Fig. 2b). The model was initialized with a nearly two-layer density stratification that resembles Sermilik Fjord in the nonsummer months (Straneo et al. 2011): the pycnocline is centered at 160-m depth and has a density difference of 1.1 kg m^{-3} , resulting in a first baroclinic mode phase speed of $c = 1.1 \text{ m s}^{-1}$. The vertical grid spacing allows for relatively high vertical resolution in the surface Ekman layer and through the pycnocline ($< 200\text{-m}$ depth) and lower resolution in the weakly stratified deep layer.

We use the default advection scheme in ROMS, which is third-order upstream horizontal advection of momentum and tracers. The model is run with a baroclinic time step of 30 s and 16 barotropic time steps between each baroclinic step. The model simulations last between 30 and 100 days, depending on the forcing. A $k\text{-}\epsilon$ vertical mixing scheme is used, implemented with the generic length scale formulation from Warner et al. (2005) and with the stability function of Kantha and Clayson (1994). The Smagorinsky scheme is used to

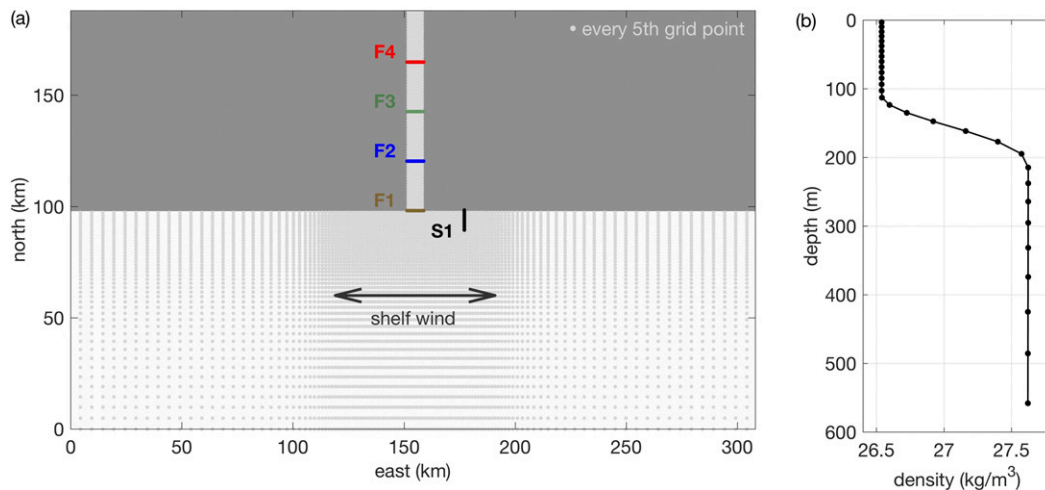


FIG. 2. (a) Domain of ROMS simulations for control run of $W = 7$ km ($W/R_d = 0.9$; similar to Sermilik Fjord), with land-masked areas in dark gray. Light gray dots are shown at every fifth grid point, illustrating the stretched horizontal grid. The ocean has a flat bottom at 600 m throughout the domain and vertical walls between ocean and land. Four sections are labeled within the fjord (from F1 to F4) and one on the shelf upstream of the fjord (S1). The arrow illustrates the orientation of shelf wind forcing, which is alongshore/east–west. (b) Initial density profile, with dots indicating the 30 vertical levels in the model.

parameterize horizontal viscosity (Griffies and Hallberg 2000), allowing for coefficients that vary with the grid spacing and with the evolving velocity field. Horizontal harmonic mixing of tracers is used to damp out gridscale noise, with coefficients that scale with the gridcell area and have a value of $12 \text{ m}^2 \text{ s}^{-1}$ for the smallest grids ($250 \text{ m} \times 250 \text{ m}$). The model contains linear bottom drag with a coefficient of $r = 3 \times 10^{-4} \text{ m s}^{-1}$.

The same boundary conditions are applied to the eastern, southern, and western boundaries: Chapman and Shchepetkin boundary conditions for the free surface and barotropic velocity, respectively (to radiate barotropic signals at the shallow-water wave speed; Mason et al. 2010), and radiation nudging for baroclinic velocities and tracers (T , S). The boundaries are nudged toward the initial stratification and zero velocity, with a nudging time scale of 2 days for inflow into the domain and 100 days for outflow. A closed, no-slip boundary is imposed between the ocean and land. Wind stress is applied over the shelf region, excluding the fjord, in the alongshore direction (Fig. 2) in order to excite Kelvin waves that will propagate into the fjord. The surface and bottom fluxes of mass and buoyancy are set to zero in all runs.

DESCRIPTION OF MODEL RUNS

Two sets of ROMS runs are used to explore the dynamics of shelf forcing across the parameter space of Greenlandic fjords.

In set A, the fjord response to periodic shelf forcing is investigated across a range of fjord geometries and forcing frequencies, with each run in set A represented

as a circle in Fig. 1. Shelf pycnocline fluctuations (Kelvin waves) are generated by a sinusoidal alongshore wind stress on the shelf. These runs are forced with seven different periods between 3 and 10 days, resulting in values of $\omega L/c$ from 0.6 to 2.1 (given a fixed fjord length of 90 km and $c = 1.1 \text{ m s}^{-1}$). The ratio of the fjord width to the deformation radius W/R_d is varied over five values between 0.2 and 3.5. For almost all of these runs, W/R_d is changed by varying the fjord width between 5 and 28 km while holding f constant at $1.3 \times 10^{-4} \text{ s}^{-1}$ (f at 65°N). To model a fjord with $W/R_d = 0.2$, however, f is reduced to 0.3×10^{-4} (f at 10°N) in order to maintain a similar resolution across the fjord without changing the model grid. The control run for set A is a 7-km-wide fjord with 6-day forcing period ($W/R_d = 0.9$; $\omega L/c = 1.0$, shown in thick red circle of Fig. 1), which is the closest representation of Sermilik Fjord.

In these periodic runs of set A, the shelf wind frequency is varied, but the wind amplitude was fixed at $\tau_S = 0.2 \text{ N m}^{-2}$. This generates periodic pycnocline fluctuations (Kelvin waves) with the same frequency as the wind forcing and with amplitudes η_S between 11 and 15 m for the various runs. We find that η_S has only a weak dependence on frequency and scales primarily with τ across the ranges of forcing frequencies, so we hold the amplitude of wind stress constant while varying the frequency in order to generate Kelvin waves on the shelf of roughly equal magnitudes across different runs. This study is not concerned with the generation of these shelf density fluctuations; instead, the focus is on the response of the fjord to imposed variability on the shelf.

Thus, in analyzing the runs, we diagnose the amplitude of the shelf heaving η_S and compare it (*not* the shelf wind) with the fjord response. Additionally, the amplitude of the fjord response scales linearly with the amplitude of the shelf wave for the range of amplitudes studied (as will be shown in section 3), so we can normalize by η_S to remove the effect of forcing amplitude variability across set A.

Set B explores the fjord response to broadband shelf forcing. Simulations are run across the same five values of W/R_d between 0.2 and 3.5 from set A (Fig. 1). Instead of forcing with a periodic wind stress, these runs are forced with a more realistic broadband time series of alongshore shelf wind. The wind field is generated by high-pass filtering a red noise time series with a cutoff period of 12 days and normalizing such that the mean is zero and the standard deviation is 0.2 N m^{-2} .

To compare these broadband runs of set B with the periodic runs in set A, we calculate the transfer function between the shelf pycnocline and the fjord response as a function of frequency. The transfer function T_{xy} is estimated as

$$|T_{xy}(\omega)|^2 = \frac{|S_{xy}(\omega)|^2}{S_{xx}(\omega)}, \quad (4)$$

where S_{xy} is the cross-spectra of the forcing x and response y , and S_{xx} is the spectra of forcing x . In this case, the forcing x is the time series of pycnocline depth on the shelf, $\eta(t)$, and the response y is the pycnocline depth or velocity in the fjord. The transfer function gives us the relationship between the shelf forcing and fjord response across the resolved frequencies in the broadband simulations.

b. Analytical models

Two simple analytical models are presented here to help interpret the numerical model and provide a framework for understanding the dynamics of shelf forcing. While both analytical models assume a two-layer fjord, one is derived for $W/R_d \ll 1$ and the other for $W/R_d \gg 1$. These two analytical models can be considered asymptotic limits, and the numerical simulations from ROMS allow us to explore the transition between regimes when $W/R_d \sim 1$, as is the case in most Greenlandic fjords (Fig. 1 and Table 1). For simplicity, both analytical models are derived assuming a periodic forcing with frequency ω , but any realistic forcing can be considered the sum of periodic forcing across a range of frequencies. Outside the fjord literature, there is a vast body of work on wave and wind forcing of estuaries, inlets, and straits that we build on to develop these analytical frameworks for studying shelf forcing in fjords.

1) 2D STANDING WAVE MODEL

A standing wave model has been used to study the barotropic response of estuaries to shelf forcing and local wind forcing (e.g., Garvine 1985; Janzen and Wong 2002; Wang 1979). These studies explore the estuarine response to shelf and local wind by neglecting cross-estuary structure and the Coriolis term in the momentum budgets, with an underlying assumption that the estuary width is much less than the barotropic deformation radius. This should be well justified for barotropic signals in mid-latitude estuaries where the barotropic deformation radius is $O(100)$ km.

Here, we modify the standing wave framework of Garvine (1985) to address the baroclinic response of a narrow two-layer fjord. By assuming that the fjord is effectively 2D, this analytical model is derived for the far left part of the parameter space in Fig. 1 where $W/R_d \ll 1$. Neglecting friction, advection of momentum, and cross-fjord flow, the along-fjord momentum and continuity equations can be written as follows:

$$h_1 \frac{\partial v}{\partial t} = c^2 \frac{\partial \eta}{\partial y} + \frac{h_2}{H} \frac{\tau}{\rho}, \quad \text{and} \quad (5)$$

$$\frac{\partial \eta}{\partial t} = h_1 \frac{\partial v}{\partial y}, \quad (6)$$

where v is the depth-averaged along-fjord velocity in the upper layer, η is the interface displacement, τ is the local wind stress, $c^2 = g'h_1h_2/H$, $g' = g\Delta\rho/\rho_0$, and $\Delta\rho$ is the density difference between layers (Fig. 3). The along-fjord momentum budget is a balance between local acceleration, pressure gradient, and wind stress. This also assumes that the interface displacements are small relative to layer thickness ($\eta \ll h_1, h_2$, so c can be treated as a constant) and that there is no mixing between layers. In R. Jackson et al. (2018, unpublished manuscript), we examine the competing roles of shelf and local wind forcing, but for now we neglect the local wind stress ($\tau = 0$) and combine Eqs. (5) and (6) to get a governing wave equation:

$$\frac{\partial^2 v}{\partial t^2} = c^2 \frac{\partial^2 v}{\partial y^2}. \quad (7)$$

Shelf forcing is communicated to the fjord through a boundary condition at the mouth such that the interface η at $y = 0$ is forced to match an imposed shelf condition. We explore the fjord response to an infinite periodic shelf forcing of the form $\eta(y = 0, t) = \eta_S e^{i\omega t}$, where ω is the frequency of the shelf forcing and η_S is the amplitude of the shelf wave. At the head of the fjord, $y = L$, the

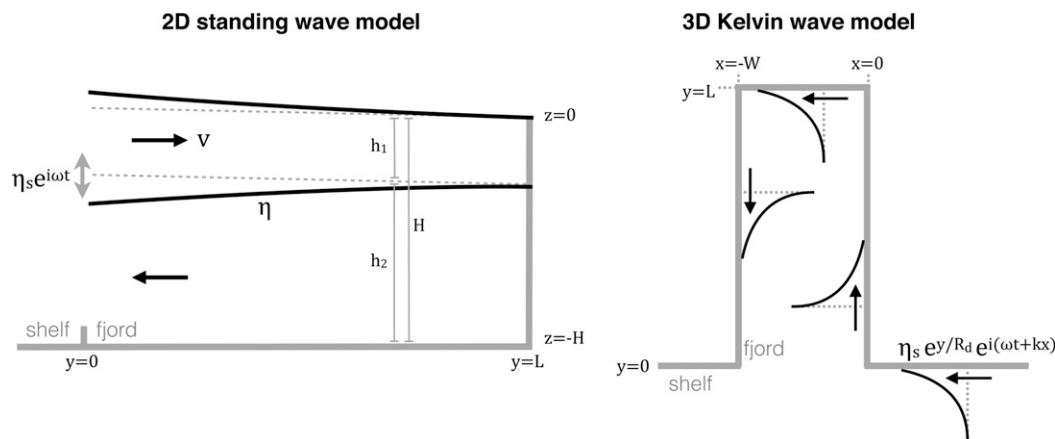


FIG. 3. (left) Schematic of the 2D standing wave model, showing depth vs along-fjord direction. (right) Schematic of the 3D Kelvin wave model, showing plan view of fjord and shelf. The amplitude of the interface displacement is projected onto the alongshore direction, illustrating the cross-shore decay of the Kelvin wave structure.

velocity is required to be zero: $v(L, t) = 0$. This gives the well-known standing wave solution:

$$\eta(y, t) = \eta_s \frac{\cos[k(L - y)]}{\cos(kL)} \cos(\omega t), \quad \text{and} \quad (8)$$

$$v(y, t) = \frac{\eta_s c}{h_1} \frac{\sin[k(L - y)]}{\cos(kL)} \sin(\omega t). \quad (9)$$

When the forcing period is long compared to the adjustment time scale (i.e., $wL/c = kL \rightarrow 0$ or $\cos kL \rightarrow 1$), this model reduces to the slab model of Arneborg (2004) for a rectangular fjord:

$$\eta(y, t) = \eta_s \cos(\omega t), \quad \text{and} \quad (10)$$

$$v(y, t) = -\frac{(L - y)}{h_1} \frac{\partial \eta_s}{\partial t} = \frac{L - y}{h_1} \eta_s \omega \sin(\omega t). \quad (11)$$

In this limit, the pycnocline heaving is uniform throughout the fjord, with the same phase and amplitude at all points. The velocity decays linearly toward the head of the fjord. The assumptions for this slab model, of small W/R_d and small $\omega L/c$, place it in the lower left corner of the parameter space in Fig. 1.

We focus the equations on the upper-layer velocity v and upper-layer volume flux Q (written without subscripts for simplicity), but since these are baroclinic flows, the lower-layer velocity and volume flux are simply related by $v h_1 = -v_2 h_2$, and $Q = -Q_2$.

2) 3D KELVIN WAVE MODEL

The second analytical model allows for lateral variability in the cross-fjord direction. This framework is inspired by a series of studies of Kelvin waves propagating through straits (e.g., Toulany and Garrett 1984;

Durland and Qiu 2003; Johnson and Garrett 2006). These studies show that, unless a strait's width is considerably narrower than the deformation radius, the majority of incident Kelvin wave energy will be transmitted through the strait, as opposed to propagating past the mouth. This suggests that for fjords with $W/R_d \sim O(1)$, the Kelvin wave propagation, including both along-coast and cross-coast structure, should be investigated.

In this model, the fjord is forced by an inviscid periodic Kelvin wave on the shelf with frequency ω and amplitude η_s :

$$\eta(x, y, t) = \eta_s e^{y/R_d} e^{i(kx + \omega t)}, \quad \text{and} \quad (12)$$

$$u(x, y, t) = \frac{c^2}{fh_1} \frac{\partial \eta}{\partial y} = \frac{c}{h_1} \eta_s e^{y/R_d} e^{i(kx + \omega t)}, \quad (13)$$

where u is the depth-averaged velocity in the upper layer on the shelf, $y = 0$ is the shelf coastline with the orientation of Fig. 3, and $-x$ is the direction of Kelvin wave propagation on the shelf. The Kelvin wave decays exponentially away from the coast with a decay scale of R_d , and it obeys the semigeostrophic equations of motion, where the along-coast momentum balance is between local acceleration and the pressure gradient, while the cross-coast momentum is in geostrophic balance. At a fixed point on the coastline ($y = 0$), the pycnocline signal is the same as the forcing signal in the standing wave model: $\eta = \eta_s e^{i\omega t}$.

To examine the response of a fjord to Kelvin waves on the shelf, we formulate a simple analytical model where periodic Kelvin waves from the shelf propagate into the fjord, around the perimeter of the fjord, and then exit freely (Fig. 3). Supported by the results of Durland and Qiu (2003), the portion of the Kelvin wave on the shelf

within a distance W (the fjord width) of the coast is allowed to turn into the fjord. Thus, if the fjord width is much larger than the deformation radius, then the entire cross-shore structure of the Kelvin wave will enter the fjord. If the cross-shore structure of the Kelvin wave is wider than the fjord width, only the portion within W of the coast will enter the fjord.

The waves on either side of the fjord are assumed to add linearly, and the waves are undistorted as they propagate around the head, as often assumed for barotropic tidal signals in large bays (e.g., Taylor 1921; Gill 1982). As the wave propagates around the head of the fjord and switches from propagating up-fjord on the right side to down-fjord on the left side, it is equivalent to reflecting the wave ($k \rightarrow -k$) and adding a phase lag of $\phi = Wk$, corresponding to the time for the wave to propagate across the width. Thus, the fjord solution for η and v can be written as the sum of an incoming and outgoing Kelvin wave:

$$\eta(x, y, t) = \eta_S e^{x/R_d} e^{i(\omega t - ky)} + \eta_S e^{-(W+x)/R_d} e^{i(\omega t + ky - 2kL - kW)}, \quad (14)$$

and

$$v(x, y, t) = \underbrace{-\frac{c}{h_1} \eta_S e^{x/R_d} e^{i(\omega t - ky)}}_{\text{incoming}} + \underbrace{\frac{c}{h_1} \eta_S e^{-(W+x)/R_d} e^{i(\omega t + ky - 2kL - kW)}}_{\text{outgoing}}, \quad (15)$$

where the fjord has dimensions of $x = [-W, 0]$, $y = [0, L]$ as illustrated in Fig. 3.

While this model accounts for the phase lag for the Kelvin wave to propagate across the width of the fjord at the head, the solutions for η and v do not describe the structure of the waves as they reflect around the head of the fjord—therefore, this solution would be invalid close to the head of the fjord [i.e., within $O(R_d)$ of the head]. Additionally, this model makes several assumptions. First, waves propagate around the head of the fjord with no dissipation of energy (though section 3c briefly examines a dissipative version of this model where the waves are entirely damped at the head). Second, the waves on either side of the fjord are assumed to add linearly. And, most importantly, it assumes that the outgoing wave does not feel the upstream boundary condition that is imposed on the incoming Kelvin wave—the outgoing wave can leave completely with a phase set by its propagation time around the fjord. As a fjord becomes sufficiently narrow, this last assumption should become problematic.

The Kelvin wave model includes both the along- and cross-fjord structure. With some manipulation and the

use of trigonometric identities, Eq. (14) for $\eta(x, y, t)$ can be rewritten as follows:

$$\eta(x, y, t) = \eta_F(x, y) \sin[\omega t + \phi_\eta(x, y)] \quad (16)$$

such that the signal at any given location is a simple sine wave of amplitude $\eta_F(x, y)$ and phase $\phi_\eta(x, y)$. These amplitude and phase functions are

$$\eta_F(x, y) = \sqrt{K^2 + M^2} \quad \text{and} \quad (17)$$

$$\phi_\eta(x, y) = \tan^{-1}\left(\frac{K}{M}\right), \quad (18)$$

where

$$K(x, y) = \eta_0 (e^{x/R_d} + e^{-(W+x)/R_d}) \cos[k(y - L - W/2)] \quad (19)$$

and

$$M(x, y) = \eta_0 (e^{x/R_d} - e^{-(W+x)/R_d}) \sin[k(y - L - W/2)]. \quad (20)$$

This manipulation allows us to examine the spatial patterns of amplitude and phase throughout the fjord (Fig. 4). In the cross-fjord direction, the amplitude of η and v are largest at the edges. In the along-fjord direction, velocity is largest at the mouth and decays toward the head, while the interface amplitude increases toward the head. Down the middle of the fjord, the amplitudes of the incident and reflected Kelvin waves are equal, such that the signal looks like a standing wave. Away from the center of the fjord, however, the waves do not balance and the signal looks partially or entirely progressive. In velocity, the cross-fjord difference in phase is largest at the head (where its amplitude is smallest), while in η the cross-fjord difference in phase is largest at the mouth (where its amplitude is smallest).

Cross-fjord-averaged quantities

For comparison with the 2D standing wave model, we compute the cross-fjord-averaged response in the Kelvin wave model. The cross-fjord averages of the pycnocline displacement and upper-layer velocity are

$$\bar{\eta}(y, t) = 2 \frac{R_d}{W} (1 - e^{-W/R_d}) \eta_S \cos[k(L + W/2 - y)] \cos(\omega t) \quad (21)$$

and

$$\bar{v}(y, t) = 2 \frac{c}{h_1} \frac{R_d}{W} (1 - e^{-W/R_d}) \eta_S \sin[k(L + W/2 - y)] \sin(\omega t), \quad (22)$$

where overbars represent cross-fjord averages.

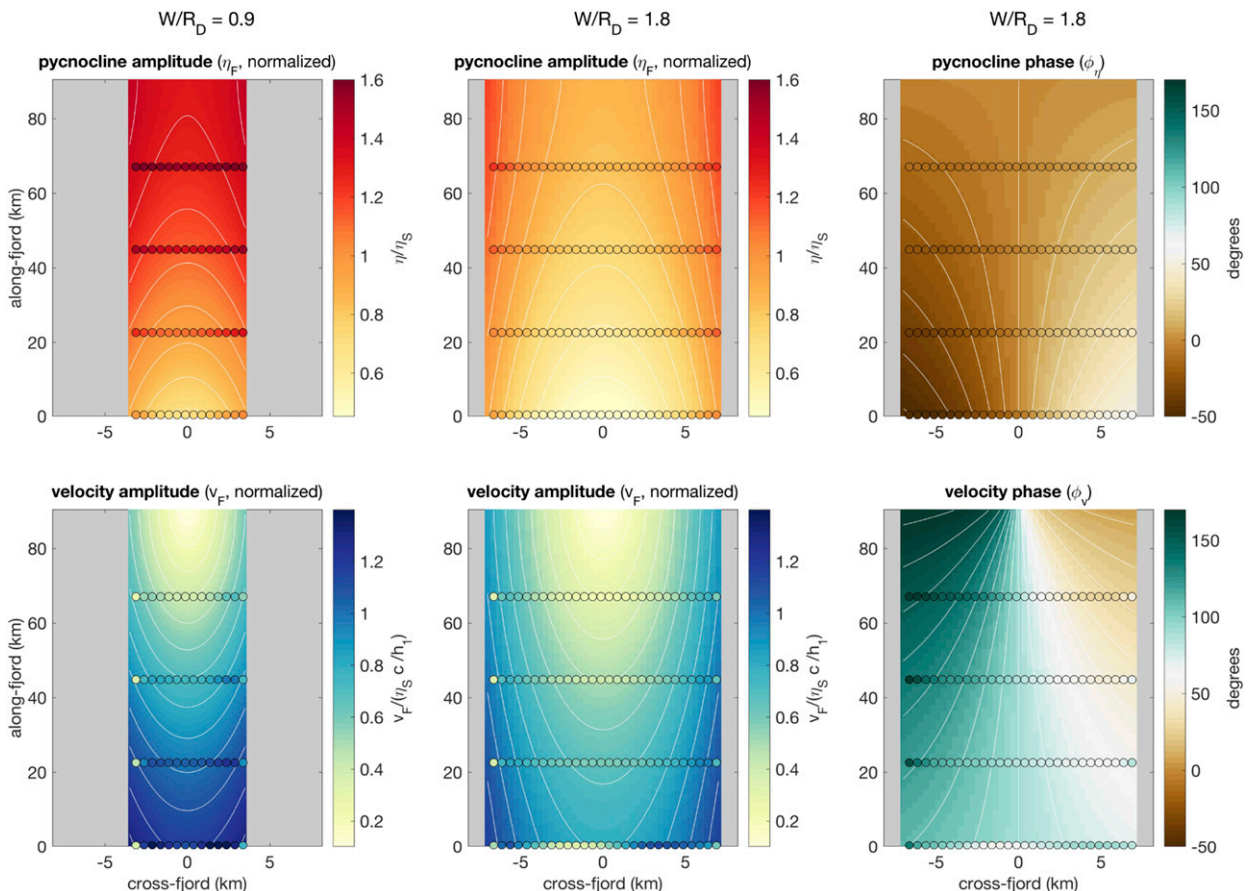


FIG. 4. Amplitude and phase for (top) pycnocline and (bottom) velocity for (left) $W = 7$ km and (center), (right) $W = 14$ km, both with $L = 90$ km, $c = 1.1 \text{ m s}^{-1}$, and $T = 6$ days. The interface amplitude is normalized by the shelf amplitude η_S , and the velocity is normalized by $\eta_S c/h_1$. The background colors with contours are from the Kelvin wave analytical model [Eqs. (16)–(20)], while circles are results from the corresponding ROMS simulations. Note: x and y axes are not to scale.

c. Contrasting behavior in 2D and 3D analytical models

Before addressing the numerical model results, the expected behavior in the limits of the two analytical models is examined. Figure 5 compares the amplitude of the fjord response in velocity and pycnocline fluctuations for the 3D Kelvin wave model [Eqs. (21) and (22)] and the 2D standing wave model [Eqs. (8) and (9)], showing that the fjord response has a very different parameter dependence in these two models. Here and at many places throughout the text, we examine the pycnocline response in the inner fjord and the velocity response at the mouth, since the pycnocline fluctuations are amplified toward the inner fjord and the velocities are largest at the mouth (Fig. 4).

In the 2D standing wave model, the fjord response is only a function of $\omega L/c$, and the amplitude of the fjord response increases as ω approaches the resonant frequency of $\omega_R = \pi c/2L$. In other words, when $\cos(kL) \rightarrow 0$

in Eq. (8), the fjord response blows up. For Sermilik Fjord conditions ($L = 90$ km; $c = 1.1 \text{ m s}^{-1}$), the resonant forcing period is 3.9 days. At low frequencies, the response plateaus to $\bar{\eta}_F/\eta_S = 1$, which is the slab model with uniform heaving throughout the fjord.

The Kelvin wave model, on the other hand, has a weaker dependence on $\omega L/c$ and a strong dependence on W/R_d . The fjord response increases as the fjord width decreases. The amplitude of the fjord pycnocline is relatively insensitive to $\omega L/c$, except for a decrease at high frequencies. The velocity response has a stronger sensitivity to $\omega L/c$, with modest amplification near the resonant forcing period, which corresponds to the incoming and outgoing Kelvin waves adding constructively. Although the cross-fjord-averaged Kelvin wave expressions [Eqs. (21) and (22)] resemble the standing wave expressions [Eqs. (8) and (9)] in their cosine terms, the Kelvin wave amplitude does not converge to the standing wave solution as $W/R_d \rightarrow 0$.

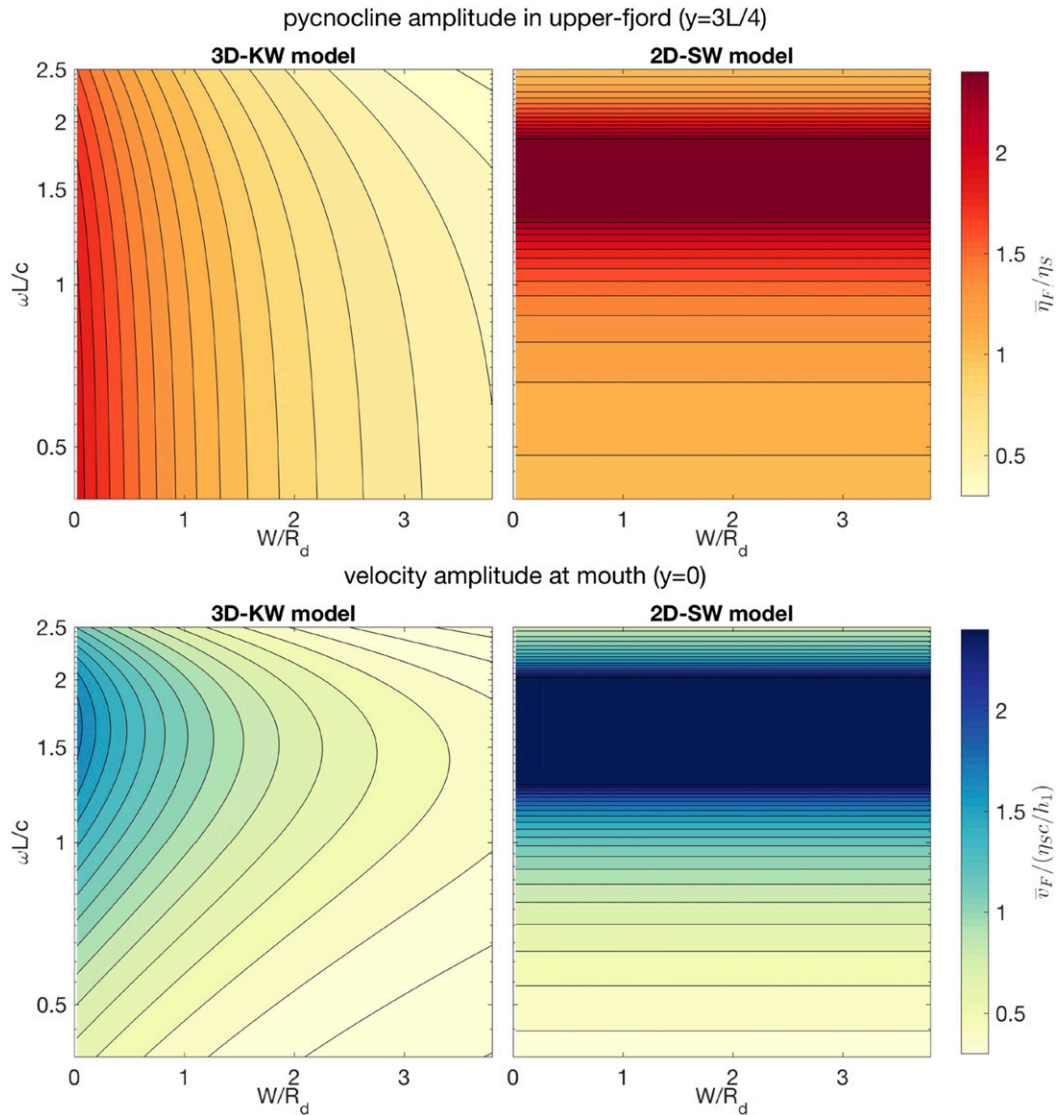


FIG. 5. (top) Amplitude of pycnocline fluctuations (cross-fjord averaged and normalized by shelf amplitude) in the inner fjord ($y = 3/4L$) and (bottom) the amplitude of velocity (cross-fjord averaged and normalized by $\eta_S c/h_1$) at the fjord mouth ($y = 0$) for the (left) 3D Kelvin wave model and (right) 2D standing wave model. Note: the color map in the standing wave panels saturates because the response goes to infinity at $\omega L/c = \pi/2 \approx 1.6$.

It should be noted that the Kelvin wave solution obeys the same along-fjord momentum budget as the standing wave model [Eq. (5)]: a balance between along-fjord pressure gradient and acceleration. The difference between these analytical models is in the mouth boundary condition and in the allowance of cross-fjord structure. For the standing wave model, the incoming and reflected wave must sum to an imposed boundary condition at the mouth. Put another way, the fjord is assumed to have no impact on the shelf. For the Kelvin wave model, the outgoing wave has no imposed boundary condition—only the incoming wave is specified. As $W/R_d \rightarrow 0$, one would

expect the boundary condition in the Kelvin wave model to be problematic. Similarly, when $W/R_d \gg 1$, the boundary condition for the standing wave model is clearly invalid.

With this expected behavior in the limit of wide and narrow fjords, the question then arises: What is the response of a fjord to shelf waves when $W/R_d \sim O(1)$, as is the case for many Greenlandic fjords? If these two simple analytical models describe the fjord response at $W/R_d \ll 1$ and $W/R_d \gg 1$, respectively, then what happens in the transition between these two regimes? And where in parameter space does that transition occur?

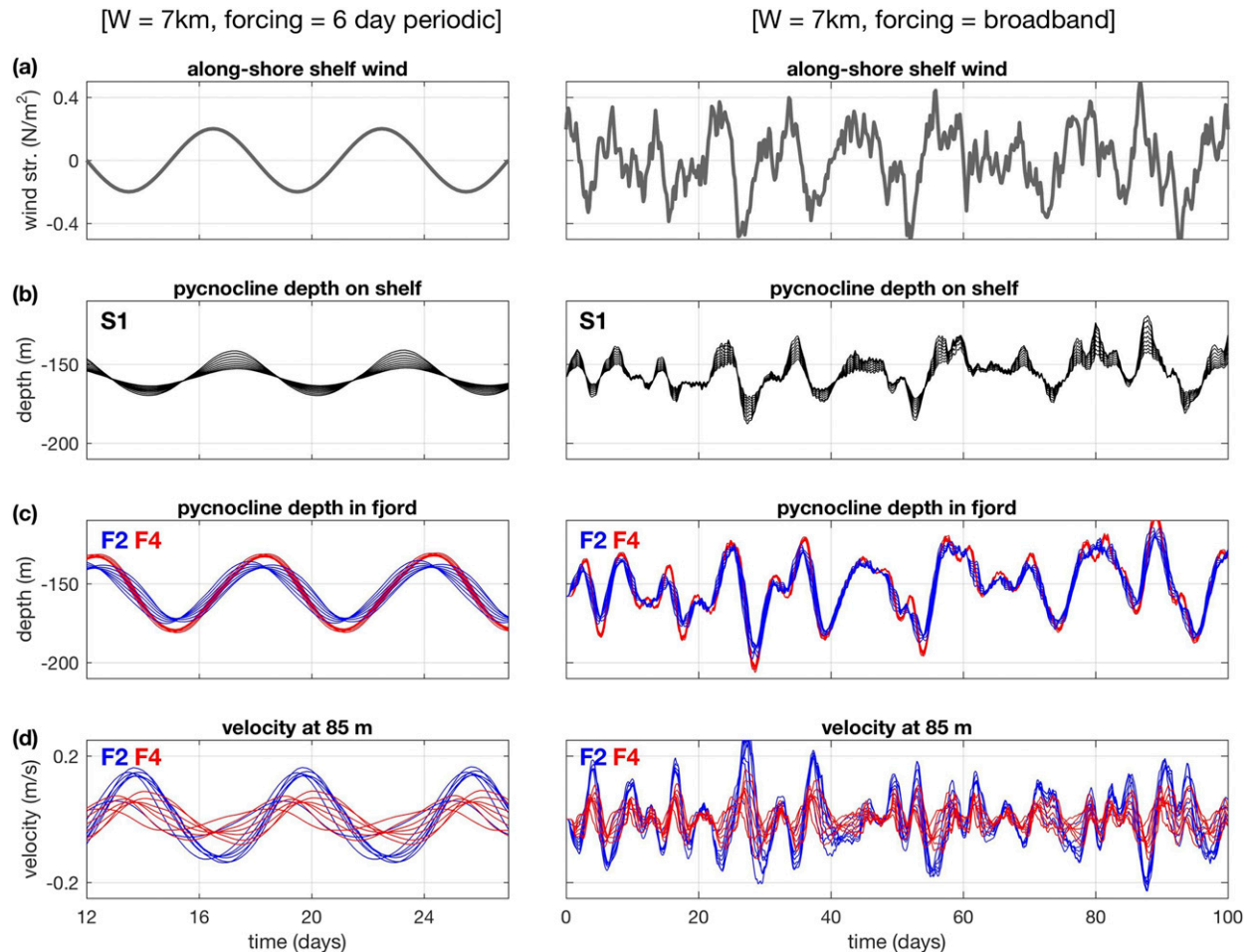


FIG. 6. (left) Control run for set A ($W = 7$ km; $T = 6$ days). (right) Control run for set B ($W = 7$ km; broadband forcing). (a) Alongshore wind, applied to the shelf region of the domain. Positive is to the east and upwelling favorable. (b) Depth of the pycnocline (defined as $\sigma = 27$ kg m $^{-3}$) on the shelf at nine points across section S1 at 1-km intervals. (c) Depth of pycnocline in fjord at sections F2 (blue) and F4 (red), at 1-km intervals across sections. (d) Velocity at 85-m depth at sections F2 (blue) and F4 (red), also every 1 km. Section locations for S1, F2, and F4 are shown in Fig. 2. Note: the left panels start at day 12 and show only a subset of the simulation; however, the simulation reaches a steady periodic solution after 1–2 days.

3. Results

a. ROMS control run with Sermilik setup and forcing

In the periodic control run for set A, with a Sermilik-like fjord of $7 \text{ km} \times 90 \text{ km}$ ($W/R_d = 0.9$), the shelf is forced by a sinusoidal along-shelf wind stress with 0.2 N m^{-2} amplitude and a 6-day period (left side of Fig. 6). The shelf wind drives heaving in the shelf pycnocline with the same 6-day periodicity. Upstream of the fjord, the amplitude of the shelf pycnocline fluctuations, η_s , is 14 m (28 m from crest to trough) at the coast and decays away from the coast, consistent with an e -folding decay scale of the deformation radius. The shelf interface is well represented by the Kelvin wave expression of $\eta(x, y, t) = \eta_s e^{y/R_d} \cos(kx + \omega t + \phi)$, where ω is the wind forcing frequency, and ϕ is a constant. In the control run for set B (right side of Fig. 6), a broadband wind field on

the shelf drives broadband Kelvin waves. Both cases represent a well-known phenomenon of shelf winds exciting internal Kelvin waves—the question of this study is how the fjord responds to these Kelvin waves on the shelf.

In both the periodic and broadband simulations, the fluctuations in the shelf pycnocline propagate into the fjord and drive heaving in the pycnocline that is modestly amplified toward the head of the fjord (Fig. 6c) and along-fjord velocities that are larger near the mouth of the fjord (Fig. 6d). In the periodic simulations, the upstream shelf matches the periodic solution predicted by theory from the beginning of the simulation, whereas the fjord reaches a steady periodic response after 1–2 days of forcing.

Throughout most of the fjord, the along-fjord velocity is in geostrophic balance (i.e., the cross-fjord momentum balance is geostrophic) and the along-fjord momentum is

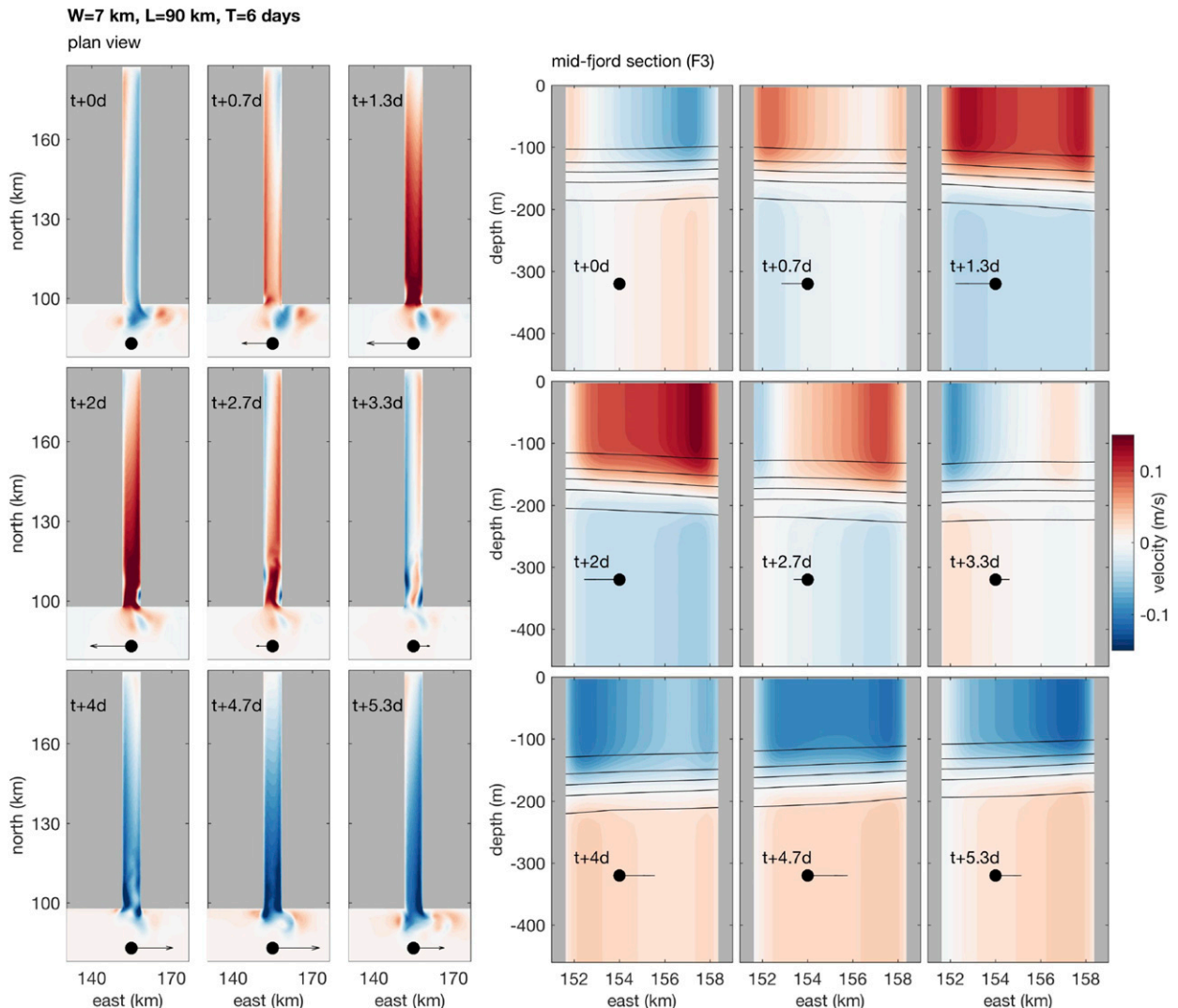


FIG. 7. Along-fjord velocity from control run of set A ($W/R_d = 0.9$; $T = 6$ days) at nine snapshots over one forcing period. (left) Plan view of northward velocity at 85-m depth, i.e., in the upper layer above the pycnocline. (right) Northward velocity at fjord cross-section F3 (see map in Fig. 2), at the same times as in the left panels. Note: only the upper 450 m is shown, while the full depth is 600 m. In both panels, black arrows show the direction of alongshore shelf wind forcing, and time in days is shown relative to $t = 12$ days from the start of the run. The first five panels have downwelling-favorable winds while the last four have upwelling-favorable winds.

dominated by the acceleration and pressure gradient terms (appendix A). At the mouth of the fjord, the along-fjord momentum balance becomes more complex.

Figure 7 shows the velocity field at nine snapshots over a six-day cycle in the periodic control run. As the pycnocline lowers, there is, for the most part, inflow in the upper layer and outflow in the lower layer. This flow reverses as the pycnocline rebounds. The velocity field is almost entirely baroclinic and decays toward the head of the fjord. While the dominant signal in the pycnocline is vertical heaving, small changes in the cross-fjord slope, on top of the heaving signal, result in lateral shear and occasional cross-fjord reversals at times of weak velocity (since along-fjord

velocity is in geostrophic balance). At the junction between fjord and shelf, the velocity field becomes more complicated with features resembling jets, eddies, or evanescent Poincaré waves (e.g., Durland and Qiu 2003).

When the fjord width is changed from 7 to 14 km (W/R_d from 0.9 to 1.8), the cross-fjord variability increases (appendix B). The velocity and interface fluctuations are more markedly trapped on the edges of the fjord. For the same shelf forcing, the fjord velocities are smaller for the wider fjord. For this wider fjord with $W/R_d = 1.8$, the Kelvin wave model predictions for the amplitude and phase of the fjord response closely match the ROMS simulations (Fig. 4). For the narrower control run with

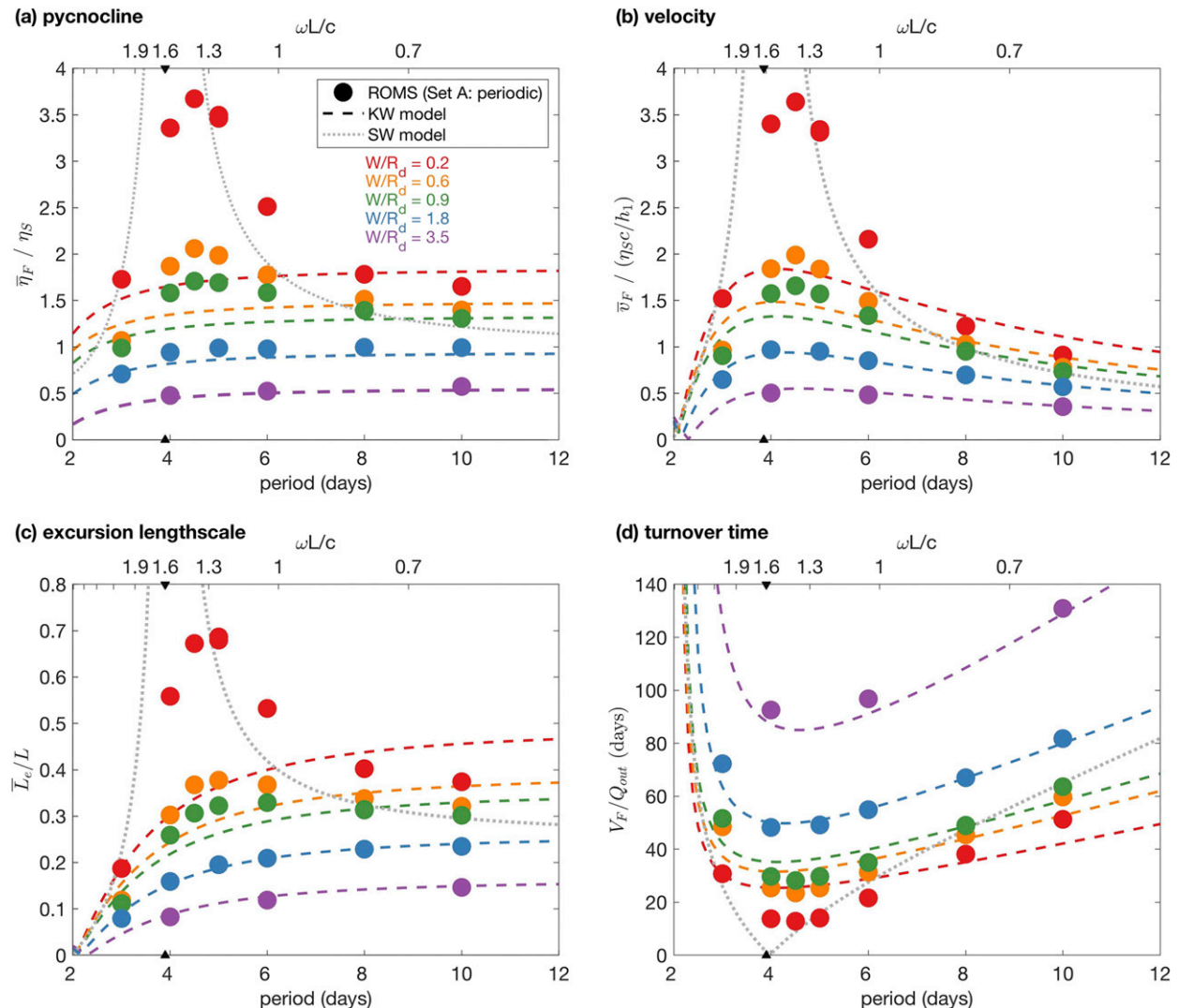


FIG. 8. Four metrics for the fjord response as a function of forcing period (or $\omega L/c$). Each dot is a ROMS simulation in set A with a different periodic forcing period and fjord geometry. Dashed colored lines are predictions from the 3D Kelvin wave model. Dotted gray lines are predictions from the 2D standing wave model. Color indicates the fjord width. (a) Amplitude of the average pycnocline fluctuation in the inner fjord at F4, normalized by the amplitude of the shelf wave η_S . (b) Amplitude of the average velocity in the upper layer at the fjord mouth (F1) normalized by η_{SC}/h_1 . (c) Excursion length scale at the fjord mouth (F1) normalized by the fjord length. (d) Turnover time, defined as fjord volume \mathcal{V}_F divided by the mean outflowing volume flux at the fjord mouth (F1). The resonant forcing period ($\omega L/c = \pi/2$) is marked on the x axis with black triangles.

$W/R_d = 0.9$, the phase propagation of the density signal is consistent with the Kelvin wave model (and this phase propagation would be absent in the standing wave model); however, the amplitude is slightly larger than expected from the Kelvin wave model.

b. Shelf-forced dynamics across the parameter space of fjords

Set A of ROMS runs are used to test the dependence of the fjord response as a function of W/R_d and $\omega L/c$. In Fig. 8a, the amplitude of the fjord pycnocline

(cross-sectionally averaged $\bar{\eta}_F$) in the inner fjord is plotted as a function of forcing period for all runs in set A. These ROMS runs (in dots) are compared with the expected response from the Kelvin wave model [Eq. (21); dashed color lines] and the standing wave model [Eq. (8); dotted gray line]. In the relatively wide fjords, with W/R_d of 1.8 and 3.5, the ROMS runs match the corresponding Kelvin wave prediction (purple, blue lines). For these runs, there is a weak dependence on the forcing period and the pycnocline amplitude increases with narrower fjords. For the narrowest runs

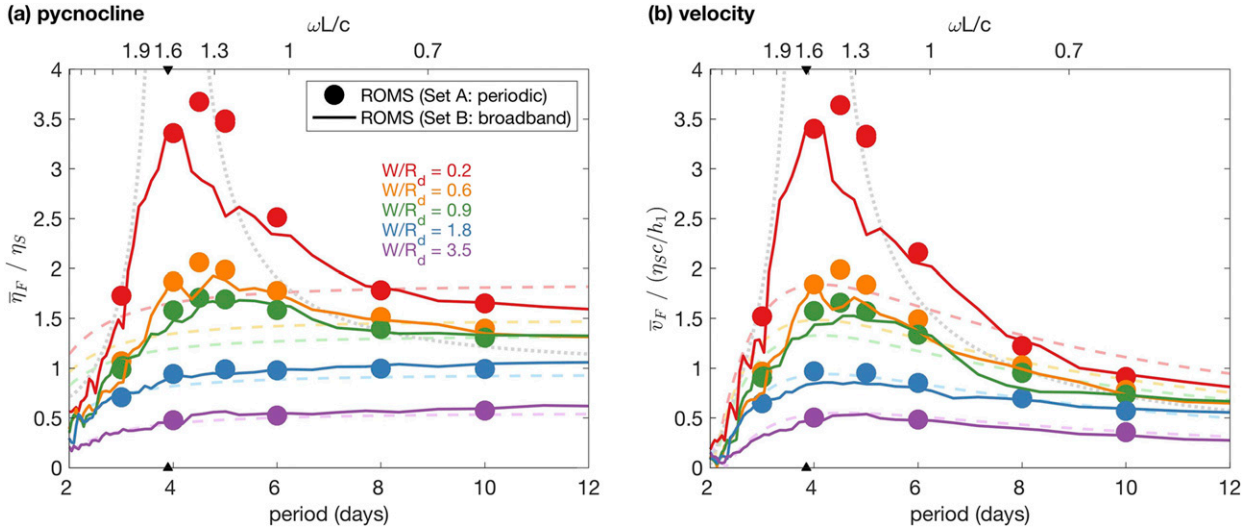


FIG. 9. As in Figs. 8a,b, with the addition of the transfer functions from broadband forcing (ROMS set B) in solid lines. (a) For periodic runs, $\bar{\eta}_F/\eta_S$ is calculated directly. For broadband runs, this quantity is estimated as $T_{\eta_S\bar{\eta}_F}$, the transfer function between η_S and $\bar{\eta}_F$. (b) For periodic runs, $\bar{v}_F/(\eta_{SC}/h_1)$ is calculated directly. For broadband runs, this quantity is estimated as $T_{\eta_S\bar{v}_F}(c/h_1)$, where $T_{\eta_S\bar{v}_F}$ is the transfer function between η_S and \bar{v}_F . Dashes and dotted lines in faded colors are the analytical predictions, as shown in Figs. 8a,b. The resonant forcing period ($\omega L/c = \pi/2$) is marked on the x axis with black triangles.

of $W/R_d = 0.2$ (red), the fjord roughly follows the standing wave prediction: the response varies strongly with the forcing frequency and becomes large (3.5 times the shelf amplitude) near the resonant frequency. Thus, the two analytical models capture the basic features of the numerical simulations for the two limits $W/R_d \leq 0.2$ and $W/R_d \geq 1.5$.

The runs with W/R_d of 0.6 and 0.9 (orange, green lines) fall in the transition between regimes: the dots for ROMS runs lie between the dashed lines for the Kelvin wave model and the dotted line for the standing wave model. There is a modest amplification near the resonant frequency, but it is far smaller than would be expected for the full standing wave solution. Instead, the response falls closer to the Kelvin wave solution, with some deviation. This is worth emphasizing: even when the fjord width is half the deformation radius, the cross-fjord structure cannot be neglected and there is not a large amplification at the resonant frequency as the 2D standing wave model would predict.

At low-frequency forcing (large forcing periods), the fjord response plateaus. This is expected from examining Eq. (21) for $\bar{\eta}$ in the Kelvin wave model: when $\omega L/c \rightarrow 0$, the amplitude of the pycnocline fluctuations is only a function of W/R_d , increasing with narrower fjords.

A similar picture emerges when the mean velocity field is examined. Figure 8b plots the amplitude of the cross-sectionally averaged velocity at the mouth \bar{v}_F as a function of forcing period. This quantity is proportional to net volume flux between the fjord and shelf in the upper layer: $Q_{\text{up}} = Wh_1\bar{v}_F$. Similar to the pycnocline response, the

velocity in wide fjords matches the Kelvin wave model, while narrow fjord simulations follow the standing wave patterns. The runs with $W/R_d = 0.6$ and 0.9 fall in between, with modest amplification near the resonant frequency. In the limit of low-frequency forcing, the fjord velocity approaches zero in all models.

In both analytical models, there is a maximum in the mean velocity at the resonant frequency, $\omega L/c = \pi/2$. In the Kelvin wave model, this peak occurs when the ingoing and outgoing Kelvin waves add together constructively. However, the model does not require that both the incoming and outgoing wave match an imposed boundary condition at the mouth—the waves are assumed to propagate around the fjord and exit freely—so there is no possibility for a resonant solution that blows up. On the other hand, in the 2D standing wave model, the sum of the incoming and outgoing wave must satisfy a single boundary condition, since by definition there is no cross-fjord variability. So, in the absence of friction, the 2D solution blows up at resonance. In ROMS, there is a modest signal of resonance for simulations with $W/R_d = 0.6$ and 0.9, suggesting a hybrid of 2D and 3D dynamics for these fjords.

The transfer functions for the broadband simulations are shown with solid lines in Fig. 9, along with the previously discussed periodic runs and analytical predictions for the pycnocline and velocity response. The broadband results align well with the periodic runs of the same W/R_d values, suggesting that the same dynamics are at play and that the broadband simulations are just a

linear sum of the fjord response at discrete forcing frequencies. This is consistent with the results of the momentum balance that show the fjord dynamics to be primarily linear, with only modest nonlinear effects at narrow fjords of $W/R_d = 0.2$ (appendix A).

The agreement between broadband and periodic simulations demonstrates that the results from the periodic runs can be interpolated and extrapolated across the (subinertial) frequency domain. Thus, to the extent that the Kelvin wave theory matches ROMS, the Kelvin wave analytical expressions [Eqs. (21) and (22)] can be considered transfer functions to relate a broadband time series of pycnocline fluctuations to the fjord response, as a function of forcing frequency. Similarly, the 2D standing wave expressions [Eqs. (8) and (9)] can be considered transfer functions for sufficiently narrow fjords where 2D dynamics are dominant.

Three metrics are now examined to assess the magnitude and structure of the exchange between the fjord and shelf that is driven by shelf forcing.

1) EXCURSION LENGTH SCALE

To explore the spatial extent of these flows and their net impact on the fjord, we examine the excursion length scale at the fjord mouth, which captures the integrated magnitude of the oscillatory flow and is defined here as the velocity integrated over half a period. For a periodic velocity field of amplitude of v_F and period T , the excursion length scale is

$$L_e = \frac{T \left(\frac{2v_F}{\pi} \right)}{2} = \frac{Tv_F}{\pi}. \quad (23)$$

Physically, it is the approximate distance that a water parcel would travel over half of a period. (Note that this is calculated for the velocity at a fixed location, so it is only an approximation of the true Lagrangian excursion.) The excursion length scale at the mouth indicates approximately how far shelf water would travel into the fjord on each pulse; or, put another way, it indicates the region of the fjord where water exits the fjord over each cycle. If the water that exits the fjord is swept away (e.g., by a coastal current such as the East Greenland Coastal Current outside Sermilik Fjord) and does not reenter the fjord with the return flow, the fjord region within an excursion length scale of the mouth would be entirely renewed over each forcing period.

While the excursion length scale is not a direct measure of the net exchange between fjord and shelf, it is likely to scale with the renewal rate of fjord waters. For example, the tidal excursion relative to the length scale of an estuary has been shown to indicate the strength of tidal dispersion (e.g., Geyer and Signell 1992).

The excursion length scale at the mouth, normalized by the fjord length, is shown in Fig. 8c. As with the velocity and interface response, the ROMS simulations match the analytical models for large and small values of W/R_d but fall in a transition regime for $W/R_d = 0.6$ and 0.9 . From the Kelvin wave model, the mean ratio L_e/L at the mouth ($x = 0$) is

$$\bar{L}_e/L = 4 \frac{R_d}{W} (1 - e^{-W/R_d}) \frac{\sin(kL)}{kL} \frac{\eta_S}{h_1}. \quad (24)$$

As can be seen in Fig. 8c, L_e/L increases with forcing period until the response plateaus at long forcing periods (i.e., small values of kL) to

$$\bar{L}_e/L \approx 4 \frac{R_d}{W} (1 - e^{-W/R_d}) \frac{\eta_S}{h_1}. \quad (25)$$

One can see that the excursion length scale increases as the shelf wave amplitude becomes large relative to the layer thickness (η_S/h_1) and as the fjord becomes narrower. For a Sermilik-like fjord, the fraction of the fjord within L_e of the mouth is about twice the ratio of the shelf amplitude to the layer thickness: $L_e/L \approx 2.5(\eta_S/h_1)$. Thus, η_S of 30 m (typical for Sermilik Fjord) would result in $L_e/L = 0.5$; that is, shelf water would travel halfway up the fjord with every pulse.

For wide fjords with $W/R_d \geq 1.5$, the effectiveness of shelf forcing is diminished for high-frequency forcing (i.e., forcing periods less than 5 days or $\omega L/c > 1.2$), while the average fjord response is almost constant across lower-frequency forcing. When W/R_d is 0.6 or 0.9, the fjord response has a small local maximum near the resonant frequency, with the amplitude rapidly decreasing for higher forcing frequencies and plateauing at lower forcing frequencies. Across all frequencies, the excursion length scale increases for narrower fjords.

2) TURNOVER TIME SCALE

The turnover time scale (Fig. 8d) is defined here as

$$T_{\text{turn}} = \mathcal{V}_F / \langle Q_{\text{out}} \rangle, \quad (26)$$

where \mathcal{V}_F is the fjord volume, and $\langle Q_{\text{out}} \rangle$ is the time average of the outflowing volume flux across the fjord's mouth. While the excursion length scale illustrates the fraction of the fjord that leaves the fjord with each pulse, the turnover time is an approximate time scale of renewal for the fjord. This turnover time is inversely proportional to the mouth velocity in Fig. 8b, so there is a minimum in the turnover time at ~ 4 -day forcing periods in ROMS and both analytical models. For fjords with $W/R_d < 1$, the turnover at this forcing period is

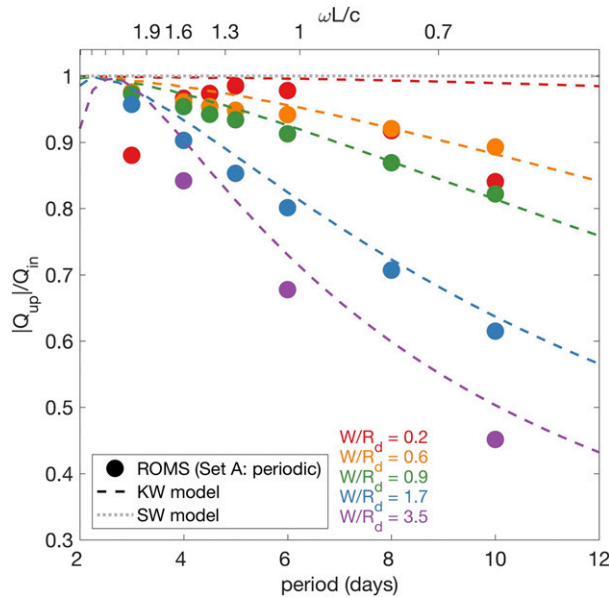


FIG. 10. Ratio of the mean absolute value of the upper-layer volume flux ($\langle |Q_{up}| \rangle$) to the mean inflowing volume flux ($\langle Q_{in} \rangle$) as a function of forcing period at midfjord (F3). ROMS runs in set A are shown in colored dots, Kelvin wave model predictions in colored dashed lines, and the standing wave model with the dotted line. Colors indicate the fjord width.

10–30 days, indicating rapid exchange with the shelf relative to the entire fjord volume.

3) LATERAL VS VERTICAL STRUCTURE

While the previous metrics have focused on cross-fjord averages, we now examine the lateral structure of the exchange. To quantify the lateral structure within the fjord, we compare the net volume flux in the upper/lower layer ($Q_{up} = -Q_{low}$) with the net volume flux that is inflow/outflowing ($Q_{in} = -Q_{out}$). If there are no cross-fjord reversals in direction, Q_{out} should equal Q_{up} or Q_{low} at all times. If there is sufficient lateral structure in the shelf-forced flows, however, the magnitude of the volume flux above/below the pycnocline might diverge significantly from the volume flux in either direction. This lateral structure might be important when thinking about the renewal of fjord waters. For example, if the water that exits the fjord is swept away (e.g., by a coastal current) so that it does not come back into the fjord with the next pulse, the mean renewal would be a function of Q_{out} , the outflowing volume flux.

In Fig. 10, the ratio ($\langle |Q_{up}| \rangle / \langle Q_{in} \rangle$) (where angle brackets are time averages) is plotted as a function of forcing frequency, with fjord width in color. For narrow fjords ($W/R_d < 1$), these quantities are approximately equal (within 15%) and the role of lateral shear in the total

volume flux is minimal. However, for fjords with $W/R_d > 1.5$, the lateral shear becomes important and the layer volume flux can be 10%–55% less than the total inflowing flux. This ratio of volume fluxes is also strongly dependent on the forcing frequency; lower-frequency forcing results in stronger lateral shear and a larger difference between layer volume flux and directional volume flux. Thus, the cross-fjord structure and lateral shear will become important for assessing the net fjord–shelf exchange for wide fjords ($W/R_d > 1$) and low-frequency forcings ($\omega L/c > 1$). The dependence of the lateral shear on fjord width and forcing period is well predicted by the 3D Kelvin wave model (dashed curves in Fig. 10) but cannot be explained by the 2D dynamics of the standing wave (dotted horizontal line).

(i) The fjord response as a function of three parameters

Overall, the fjord response to shelf forcing can be summarized in terms of the three nondimensional parameters, W/R_d , $\omega L/c$, and η_S/h_1 , as shown in Fig. 11. The excursion length scale has a relatively weak dependence on the forcing frequency, except at large values of $\omega L/c$ (i.e., high-frequency forcing). The fjord response is strongly dependent on W/R_d and linear with η_S/h_1 . It should be emphasized that the L_e/L ratios are large, in the range of 0.2–0.6 for the parameter values that are expected around Sermilik and other Greenlandic fjords. If the excursion length scale at the mouth is a decent proxy for exchange between fjord and shelf, these results suggest that a significant fraction of the fjord is flushed over each cycle of shelf forcing.

For all four metrics in Fig. 8, the fjord response and fjord–shelf exchange increases for narrower fjords and is linear with η_S/h_1 . However, the fjord response has a different frequency dependence for the different metrics. When considering the mean velocity at the mouth or the turnover time, shelf forcing is most effective around the resonant forcing period (in both narrow and wide limits) and drops off at high and low frequencies. When considering the excursion length scale, however, the fjord response increases at low frequencies (for $W/R_d \geq 0.6$). Thus, the answer to the question of what forcing frequency drives the largest fjord response will depend on the metric of interest. The excursion length scale is likely to reflect the spatial extent of rapid flushing from the shelf forcing, while the velocity scales with the total volume flux exchanged. None of these metrics, as evaluated from the idealized simulations or analytical model, can directly answer the question of net fjord renewal or tracer transport (see discussion in section 4). Instead, these metrics allow us to explore the

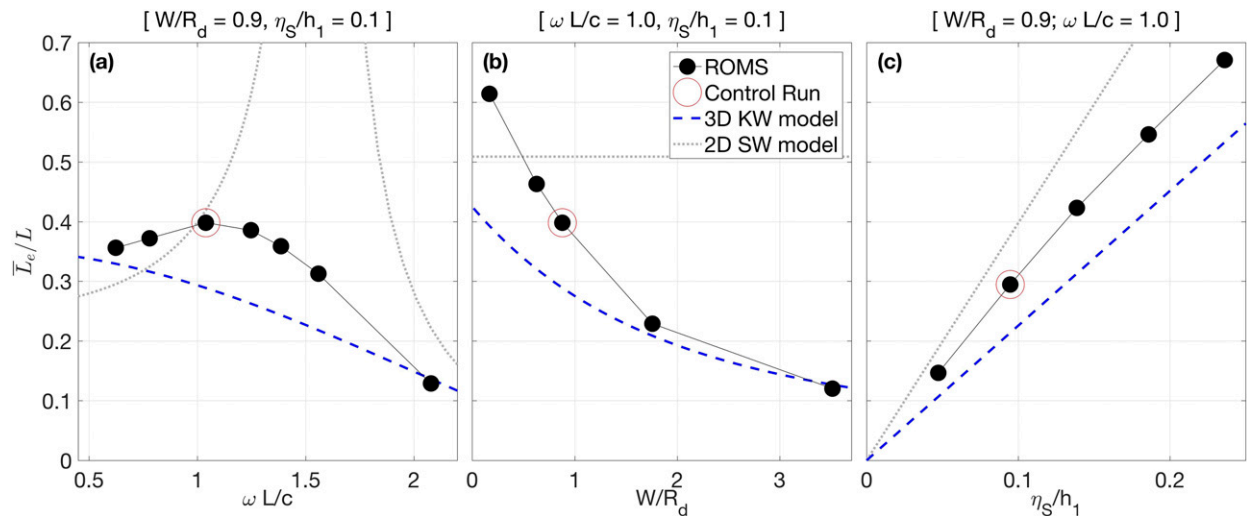


FIG. 11. Mean excursion at the mouth, normalized by L , as a function of (a) $\omega L/c$, (b) W/R_d , and (c) η_S/h_1 . In each panel, the other two parameters are held constant at the control run values of $\omega L/c = 1$, $W/R_d = 0.9$, and $\eta_S/h_1 = 0.1$. The control run is shown in each panel with a red circle. Predictions from the Kelvin wave model are shown in dashed blue and from the standing wave model in dotted gray.

basic dynamics of the fjord response as a function of fjord geometry, stratification, and forcing signal.

(ii) *Best fit between ROMS and theory*

It has been shown that neither analytical model can fully describe the shelf-forced flows as a fjord transitions through the $W/R_d \sim O(1)$ regime. However, the analytical predictions in Figs. 8–11 show that the Kelvin wave model is best at capturing the parameter dependence of the fjord's response as a function of $\omega L/c$, W/R_d , and η_S/h_1 . To quantify the relative accuracy of the

analytical models at predicting the volume flux between fjord and shelf, Fig. 12 shows the ratio of the mean velocity at the mouth in ROMS versus the analytical models, as a function of W/R_d . One can see that the 3D Kelvin wave model does relatively well at predicting the numerical results (within 30%) for $W/R_d \geq 0.6$, the parameter space of most Greenlandic fjords. On the other hand, the 2D standing wave model significantly overpredicts the numerical results in this same parameter range. Near the resonant forcing period (4 days), the Kelvin wave model underpredicts the ROMS results in

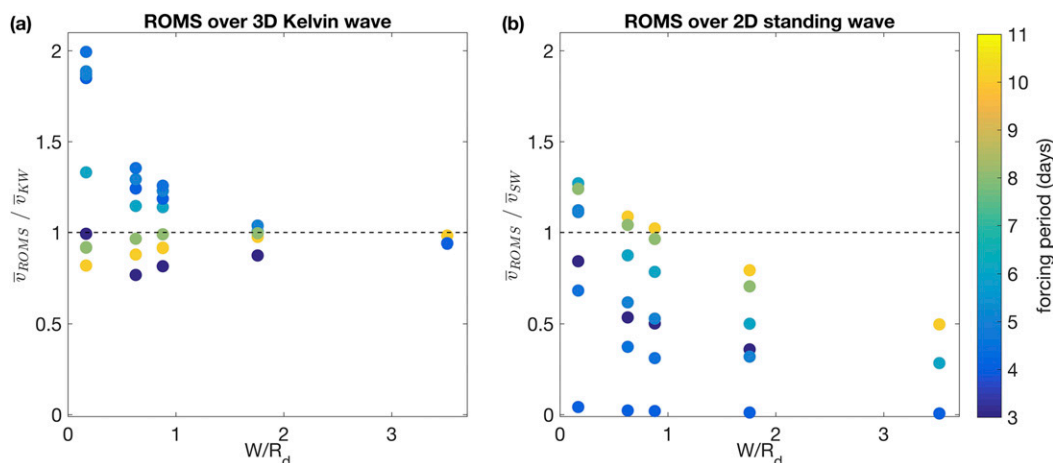


FIG. 12. Ratio of cross-fjord average velocity amplitude at the mouth from ROMS over the analytical models, as a function of W/R_d : (a) ROMS over the Kelvin wave model prediction and (b) ROMS over the standing wave model prediction. The horizontal black line indicates where the ratio equals one (i.e., exact match between analytical prediction and ROMS). Colors indicate the forcing period (days).

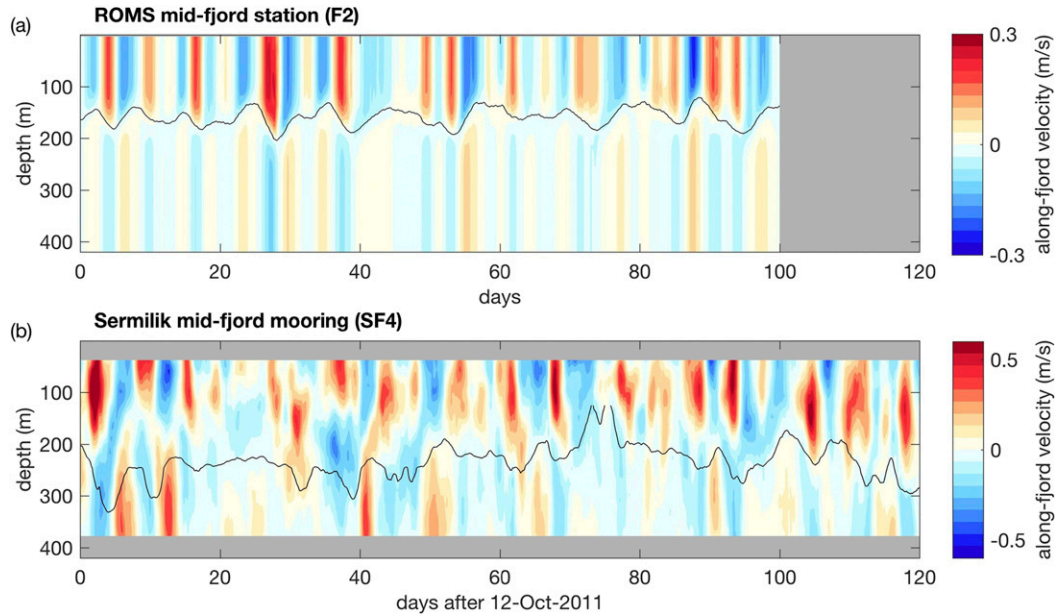


FIG. 13. (a) Along-fjord velocity at center of section F2 (location in Fig. 2) for the ROMS simulation with broadband shelf forcing and $W/R_d = 0.9$. (b) Along-fjord velocity from midfjord mooring in Sermilik Fjord (see details in Jackson and Straneo 2016; Jackson et al. 2014) over a 100-day period starting on 11 Oct 2011 (full records used in Figs. 14 and 15 cover 241 days in nonsummer months). Location of records within the fjord is approximately the same in both panels. The black line is an isopycnal of $\sigma = 27.2 \text{ kg m}^{-3}$ in (a) and $\sigma = 27.0 \text{ kg m}^{-3}$ in (b).

narrow fjords, while the standing wave model overpredicts the ROMS results in wide fjords. Overall, in the parameter space of W/R_d between 0.6 and 3.5 and $\omega L/c$ between 0.5 and 2, the Kelvin wave model generally captures the nature of the fjord response, both in its spatial structure throughout the fjord and in the mean properties.

c. Comparing the model with Sermilik observations

The ROMS control run of the broadband forcing set ($W/R_d = 0.9$) is compared with moored observations from Sermilik Fjord (Jackson et al. 2014; Jackson and Straneo 2016) in Fig. 13. The basic features of the observations are replicated in the ROMS simulation: a two-layer flow with peak energy on synoptic time scales and vertical heaving of the pycnocline, with velocity and density approximately in quadrature. In both the model and observations (which includes an inner fjord mooring; not shown), the velocity decays toward the head of the fjord and the pycnocline fluctuations are modestly amplified.

In Fig. 14, the relationship between shelf density and fjord response is examined for the observations, ROMS, and the analytical models. For this comparison, ROMS and the analytical models are evaluated at the location of the Sermilik shelf and fjord moorings. To characterize the forcing signal, η_s , in the observations, we use a

moored CTD at 290-m depth on the shelf, slightly upstream of the fjord mouth (Jackson et al. 2014; Harden et al. 2014). This provides a record, concurrent with the midfjord velocity observations in Fig. 13b, of density on the shelf at a fixed depth $\rho_{z=290}(t)$. However, for comparison with the model and theory, we want a time series of pycnocline depth $\eta_s(t)$. To estimate this quantity, we use the time series from an array of six moored CTDs between 125- and 656-m depth at the midfjord moorings, which allows us to interpolate the depth of the pycnocline in the fjord, approximated by the isopycnal of $\sigma = 27.0 \text{ kg m}^{-3}$. At the midfjord moorings, we compare the depth of pycnocline $\eta_{\sigma=27}(t)$ to the density at 290-m depth $\sigma_{z=290}(t)$. We find these quantities are linearly related with a slope of $292 \text{ m}^2 \text{ kg}^{-1}$ and a regression coefficient of $R^2 = 0.90$. We then use this linear fit to convert the density at 290m on the shelf into a time series of pycnocline depth on the shelf. This assumes that the mean density stratification on the shelf matches the mean density stratification within the fjord. Although this is a crude approximation, it is broadly consistent with the surveys of Sermilik Fjord that show a weak or nonexistent mean horizontal density gradient between the fjord and shelf (Sutherland et al. 2014). In this way, we convert our record of density on the shelf into a time series of pycnocline depth on the shelf, $\eta_s(t)$, and compare it to the fjord velocity in the

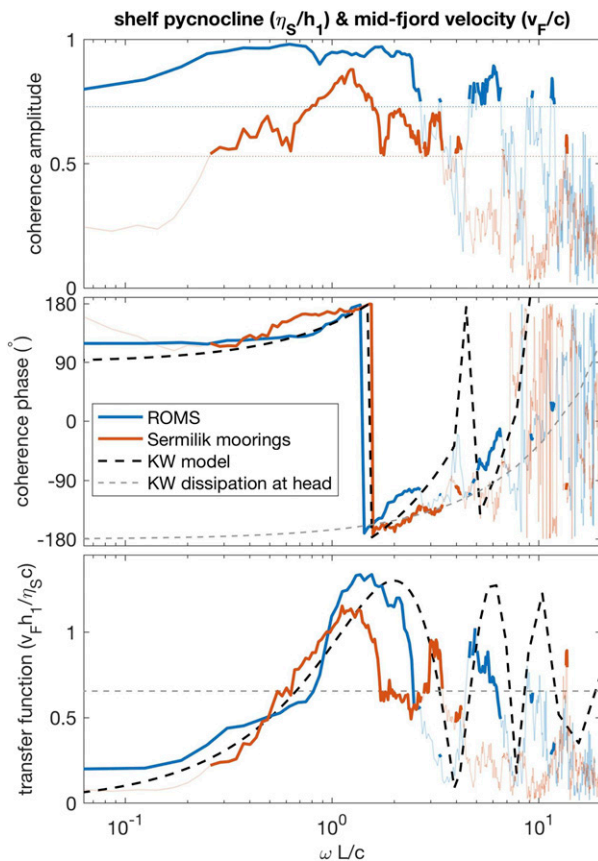


FIG. 14. (top) Coherence amplitude, (middle) coherence phase, and (bottom) transfer function between the shelf pycnocline (normalized as η_S/h_1) and midfjord velocity (normalized as v_F/c), as a function of frequency (normalized as $\omega L/c$). Blue lines are from the ROMS control run with broadband forcing, and orange lines are from Sermilik Fjord observations (241-day records). The dotted horizontal lines in the top panel indicate the level of significance at 95% confidence. In all panels, frequencies with significant coherence amplitudes are shown in thicker lines. The black dashed line is from the standard Kelvin wave model, which includes no dissipation, while the gray dashed line is a modified Kelvin wave model where the waves are assumed to entirely dissipate at the head of the fjord. In the bottom panel, the Kelvin wave model and ROMS lines are similar to the blue quantities shown in Fig. 9b, except they are evaluated here at F2 within the fjord instead of F1 at the mouth (and the orientation and scaling of the x axis is different).

upper layer $v_F(t)$, so that the analysis is analogous to the calculations from ROMS and the analytical models in previous sections. We use moored observations covering 241 days (nonsummer months in 2011–12) for spectral analysis, while Fig. 13 shows only a 100-day subset of this record.

The Sermilik observations, ROMS, and Kelvin wave model all show similar patterns in coherence amplitude and phase between the shelf pycnocline and fjord velocity (Figs. 14a,b). In both the observations and ROMS,

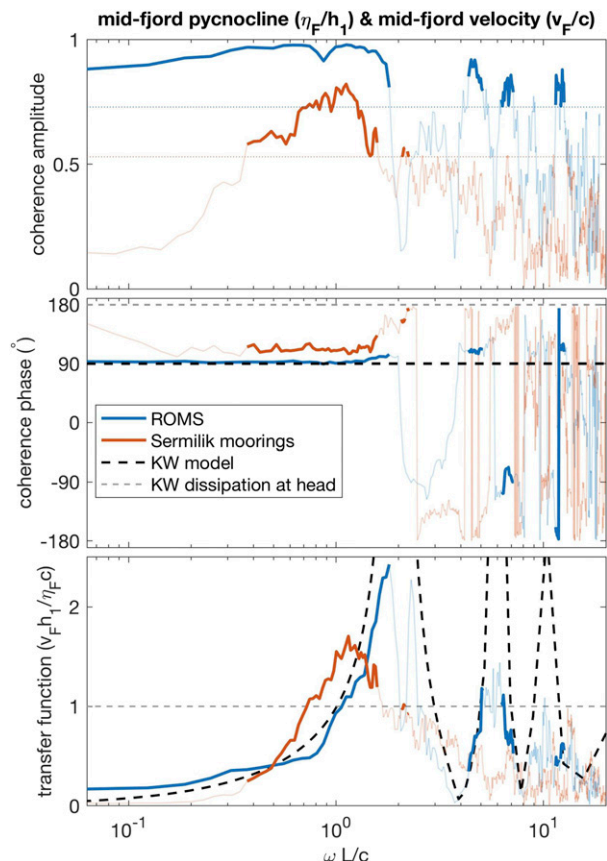


FIG. 15. As in Fig. 14, but with the pycnocline at midfjord instead of the pycnocline on the shelf; i.e., this plot examines the relationship between the pycnocline and velocity at the same mid-fjord location.

the shelf pycnocline and fjord velocity are significantly coherent for values of $\omega L/c$ between 0.3 and 3.0, corresponding to forcing at 2–24-day periods. The ROMS simulations also show coherence between shelf and fjord at lower frequencies. Where there is a statistically significant coherence, the phase matches remarkably well between the observations and models, suggesting that the models accurately represent wave propagation from the shelf into the fjord.

The observations and models also display similar features in the transfer function between shelf pycnocline and fjord velocity (Fig. 14c): the fjord velocity has a maximum response at $\omega L/c$ between 1.2 and 2 (3–5-day forcing periods) and goes to zero at low-frequency forcing. The peak in the observations is smaller and offset to lower frequency. This frequency offset could be a result of the choice of L , which is somewhat arbitrary for Sermilik Fjord since it splits into three branches near the head of the fjord.

At high-frequency forcing (<2-day forcing periods), the coherence between fjord and shelf is, for the most part, not

statistically significant, and the phase and transfer function are erratic. The Kelvin wave analytical model predicts several local maxima in the fjord response at these high frequencies, but the assumptions of the analytical model (e.g., subinertial) are no longer valid and this part of the frequency domain is beyond the scope of our study.

To further compare the observations, ROMS, and theory, Fig. 15 shows the relationship between pycnocline displacement and velocity at the same midfjord location. Over the synoptic time band of $\omega L/c \leq 1$, the pycnocline and velocity are exactly in quadrature for both the Kelvin wave model and the ROMS simulation. Down the center axis of the fjord where these quantities are evaluated, the ingoing and outgoing Kelvin waves add evenly such that the signal looks like a standing wave with density and velocity 90° out of phase. The observations show a similar relationship, with a steady phase of $110^\circ \pm 10^\circ$ over the coherent periods of $\omega L/c = 0.3\text{--}1.6$ (4–24-day periods).

Several studies have suggested that Kelvin waves (or coastal trapped waves) dissipate significantly within fjords, particularly at the head of fjords (Proehl and Rattray 1984; Fraser and Inall 2018). To evaluate this possibility in Sermilik Fjord, we consider a variation of the Kelvin wave model where the waves are assumed to completely dissipate at the head of the fjord. In this case, the fjord response is entirely described by the incoming Kelvin waves [the first terms in Eqs. (14) and (15)], and this solution is shown with light gray dashed lines in Figs. 14 and 15.

In the phase and transfer function, we can see that the dissipative solution is drastically different from the observations. The standard, inviscid Kelvin wave model and the observations both show a strong frequency dependence in the transfer functions, while the dissipative model is constant with frequency. In the phase relationship between fjord pycnocline and fjord velocity (Fig. 15b), the inviscid model predicts a 90° phase lag down the fjord centerline while the dissipative model has a phase lag of 180° . The observations (at $110^\circ \pm 10^\circ$) are closer to the inviscid solution. The difference between the observations and the inviscid solution could be explained by modest dissipation within the fjord ($\sim 20\%$ damping of the outgoing wave's amplitude) or by the mooring being slightly off center. At the mooring's location, the theoretical phase lag between density and velocity is 45° on the west side of the fjord, 90° down the center, and 135° on the east side. Thus, the mooring being slightly off from the dynamical center could explain the 20° deviation from quadrature, as could a modest amount of dissipation.

Overall, the observations are much closer to the inviscid Kelvin wave limit than the model with wave dissipation at the head of the fjord (Figs. 14 and 15),

suggesting that the majority of Kelvin wave energy is reflected back out of the fjord. In other words, the incoming and outgoing waves must have similar amplitudes in order to explain the observations, and dissipation does not appear to play a dominant role in Sermilik Fjord.

In summary, there are similar patterns in coherence amplitude, phase, and transfer functions across the observations, inviscid Kelvin wave model, and ROMS simulations. The observations are consistent with the theory and modeling results of the previous sections, suggesting that shelf forcing in Sermilik Fjord can largely be explained with 3D Kelvin wave dynamics.

4. Discussion

a. Transition across $W/R_d \sim O(1)$

Our results from section 3 illustrate that the Kelvin model is a better fit to the ROMS simulations than the standing wave model, for all but the narrowest runs of $W/R_d = 0.2$ (Fig. 12). However, in the transition through $W/R_d \sim 1$, the fjord response cannot entirely be explained by the Kelvin predictions and instead suggests a hybrid of 2D and 3D dynamics. For example, around $W/R_d = 0.9$, the fjord response is a strong function of its width, as the Kelvin wave model predicts, but there is also a modest amplification near the resonant forcing period that implies a role of 2D standing wave dynamics (Figs. 8 and 11).

Here, we attempt a simple explanation for the transition from the 2D standing wave model to the 3D Kelvin wave model. The forcing and fjord response are decomposed into a component of the standing wave (SW) and Kelvin wave (KW) solutions. The forcing Kelvin wave from the shelf has amplitude η_S at the coast (i.e., the shelf pycnocline is $\eta = \eta_S e^{y/R_d} e^{i(kx+ot)}$), and we can decompose that amplitude into two components:

$$\eta_S = \underbrace{\eta_S e^{-W/R_d}}_{\eta_{S_{SW}}} + \underbrace{\eta_S (1 - e^{-W/R_d})}_{\eta_{S_{KW}}}, \quad (27)$$

where $\eta_{S_{KW}}$ is the difference in the pycnocline displacement across the fjord width after the wave turns into the fjord, and $\eta_{S_{SW}}$ is the remainder of the Kelvin wave amplitude that is constant across the fjord, as illustrated in Fig. 16c. We assume now that $\eta_{S_{SW}}$ is the portion of the shelf wave amplitude that goes into forcing a standing wave response, and $\eta_{S_{KW}}$ is the portion of the shelf wave amplitude that goes into forcing a Kelvin wave response. The fjord response (written as cross-fjord averages $\bar{\eta}$ and \bar{v}) is the sum of the SW and KW solutions [Eqs. (8), (9), (21), and (22)], where the shelf forcing amplitude is $\eta_{S_{SW}}$ and $\eta_{S_{KW}}$, respectively:

$$\bar{\eta} = \underbrace{(\eta_S e^{-W/R_d}) \frac{\cos[k(L-y)]}{\cos(kL)}}_{\eta_{SW}} \cos(\omega t) + \underbrace{[\eta_S(1 - e^{-W/R_d})] 2 \frac{R_d}{W} (1 - e^{-W/R_d}) \cos[k(L + W/2 - y)] \cos(\omega t)}_{\eta_{KW}}, \quad \text{and} \quad (28)$$

$$\bar{v} = \underbrace{(\eta_S e^{-W/R_d}) \frac{c}{h_1} \frac{\sin[k(L-y)]}{\cos(kL)}}_{v_{SW}} \sin(\omega t) + \underbrace{[\eta_S(1 - e^{-W/R_d})] 2 \frac{c}{h_1} \frac{R_d}{W} (1 - e^{-W/R_d}) \sin[k(L + W/2 - y)] \sin(\omega t)}_{v_{KW}}. \quad (29)$$

As W/R_d goes to zero, there is little cross-fjord variability in the portion of the Kelvin wave that fits into the fjord, so the KW model contribution goes to zero and this hybrid model converges to the SW model. As W/R_d becomes large, the hybrid model converges to the KW model. Across the transition of $W/R_d \sim 1$, this model (if valid) can be used to assess the relative contribution of the KW and SW dynamics to the total response.

Figures 16a and 16b show the hybrid model's prediction for the fjord pycnocline and velocity amplitude, as a function of W/R_d and $\omega L/c$. A frictional time scale of 2 days has been included in the standing wave model so that the solution does not become infinite at the resonant frequency. The hybrid model's behavior can be seen as a combination of the separate analytical models in Fig. 5. Color circles overlaid in Fig. 16 show the fjord response in the ROMS simulations. One can see that this hybrid model captures the basic parameter dependence of the ROMS results across the parameter space. The fjord pycnocline and velocity response increases for narrower fjords and as the forcing frequency approaches resonance ($\omega L/c = \pi/2$). The amplification at the resonant frequency is strongest for the narrowest fjords but still has a modest impact on fjords of $W/R_d \sim 1$.

With this hybrid analytical model, we can quantify the fraction of the fjord response that comes from 3D Kelvin wave dynamics and the fraction that comes from 2D standing wave dynamics. Figure 16d plots the fraction of the velocity response from the KW component. Values of this fraction greater than 0.5 (red) indicate that the KW contribution is greater than half of the total response, while values less than 0.5 (blue) indicate that the SW contribution is larger. The 2D SW dynamics are only dominant for a narrow portion of the parameter space where $W/R_d < 0.5$. The one exception to this is around the resonant forcing frequency, where the 2D dynamics have an outsized impact. The location of eight Greenlandic fjords in this parameter space (from Fig. 1) are shown in rectangles, with Sermilik Fjord in bold. Most of these Greenlandic fjords lie on the red side of the transition region, where the KW contribution is slightly larger but the fjord behavior is

influenced by both 2D and 3D dynamics. None of the fjords lies in the region that is dominated by 2D dynamics.

In the limit of small $\omega L/c$, the fraction of the KW contribution to the total response (in both velocity and pycnocline displacement) is only a function of W/R_d :

$$\frac{\eta_{KW}}{\bar{\eta}} = \frac{v_{KW}}{\bar{v}} = \left[1 + \frac{W}{2R_d} \frac{e^{-W/R_d}}{(1 - e^{-W/R_d})^2} \right]^{-1} \approx 1 - e^{-W/R_d}. \quad (30)$$

Similarly, the fraction of the standing wave contribution is $v_{SW}/\bar{v} \approx e^{-W/R_d}$. Thus, the transition from 2D standing wave dynamics to 3D Kelvin wave dynamics occurs around $e^{-W/R_d} \approx 0.5$. The exponential decay of the Kelvin wave's cross-shore structure is integral to understanding the transition from 2D to 3D dynamics.

b. Comparing results with previous fjord studies

Our results suggest that the Kelvin wave model is a relatively good approximation for fjords with $W/R_d > 0.5$. From this model [Eq. (22)], the amplitude of the cross-fjord-averaged velocity in the upper layer is

$$\bar{v}_F = 2 \frac{c}{h_1} \frac{R_d}{W} (1 - e^{-W/R_d}) \sin(\omega L/c) \eta_S, \quad (31)$$

at the fjord mouth, for a fjord forced by a periodic Kelvin wave of amplitude η_S and frequency ω . This relationship has also been shown to represent a transfer function between a broadband forcing signal $\eta_S(t)$ and the fjord response $v_F(t)$:

$$\hat{v}_F(\omega) = 2 \frac{c}{h_1} \frac{R_d}{W} (1 - e^{-W/R_d}) \sin(\omega L/c) \hat{\eta}_S(\omega), \quad (32)$$

where $\hat{\eta}_S(\omega)$ and $\hat{v}_F(\omega)$ are Fourier transforms of $\eta_S(t)$ and $v_F(t)$. We have shown that the fjord response is dependent on both W/R_d and $\omega L/c$ in a way that cannot be explained by 2D dynamics.

Now we turn to the empirical relationship from Aure et al. (1996), which has recently been used to estimate the shelf-driven transport in Greenlandic and Norwegian fjords (e.g., Sutherland et al. 2014; Inall et al. 2015).

hybrid SW-KW model

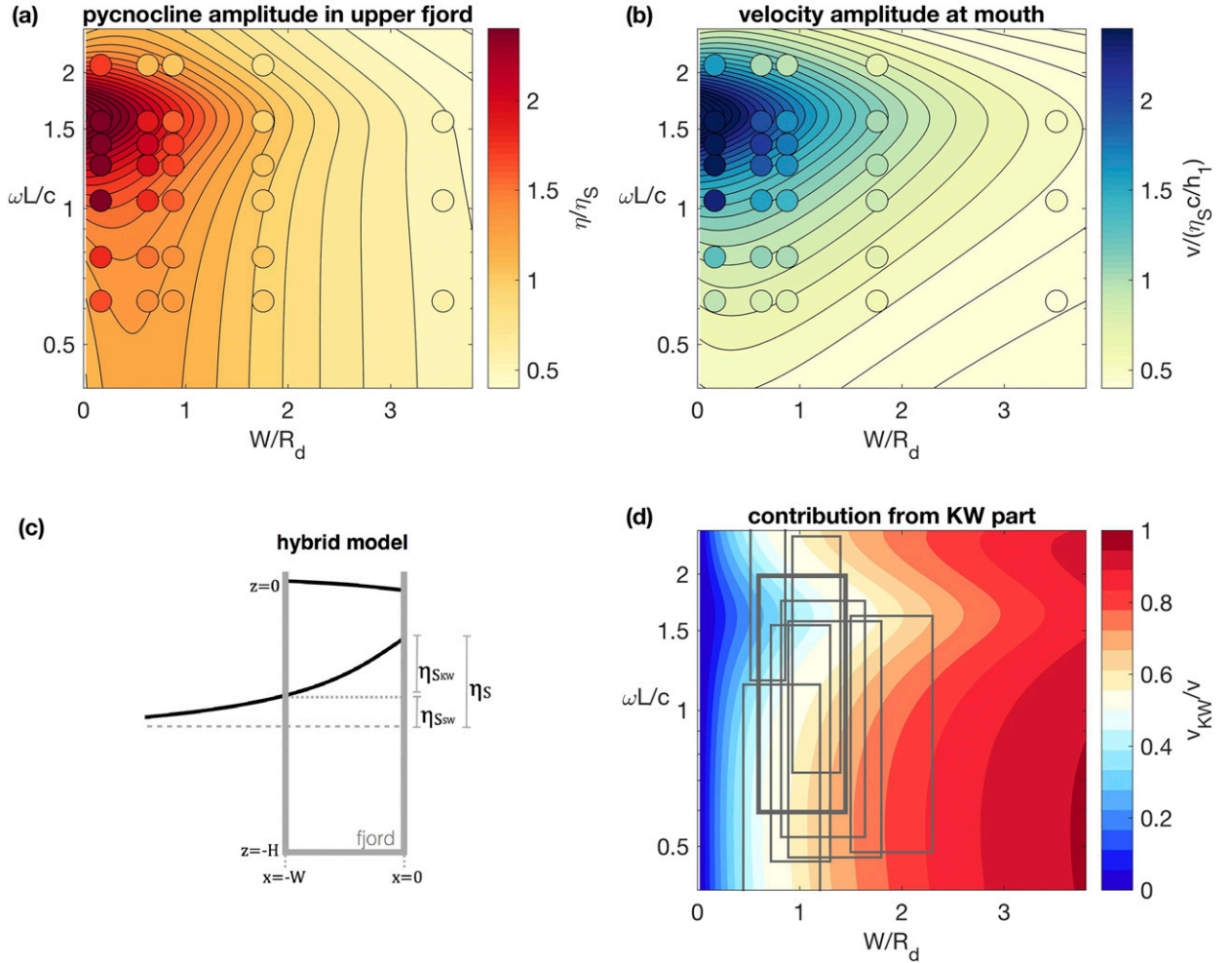


FIG. 16. Hybrid model of standing wave and Kelvin wave models. (c) Schematic of hybrid model decomposition, showing the pycnocline displacement for a Kelvin wave that has just turned into the fjord. The total amplitude of the Kelvin wave on the shelf η_S is decomposed into a component that forces the 2D standing wave model η_{SW} and a component that forces the 3D Kelvin wave model η_{KW} . (a) The background color is the hybrid model prediction for the mean pycnocline amplitude in the inner fjord ($y = 3/4L$ or F4) normalized by total forcing amplitude η_S . Circles are results from ROMS runs in set A. (b) The background color is the hybrid model prediction for mean velocity amplitude at the mouth ($y = 0$ or F1), normalized by $\eta_S c/h_1$. Circles are results from ROMS runs in set A. (d) The fraction of the fjord velocity response that comes from the KW contribution to the hybrid model. In red regions, the KW contribution is larger than the SW contribution ($\eta_{KW} > \eta_{SW}$); in blue regions, the SW contribution dominates; and white is the transition where KW and SW contributions are equal. Gray rectangles show the same eight Greenlandic fjords from Fig. 1.

For a rectangular two-layer fjord with sinusoidal shelf pycnocline fluctuations of amplitude η_S , the mean velocity between fjord and shelf predicted by Aure et al. (1996) in Eq. (1) reduces to

$$\bar{v}_F = \frac{\beta}{h_1} \sqrt{HL \frac{g' \eta_S}{\sqrt{2}}}, \quad (33)$$

using $g\Delta M/\rho = g' \eta_S/\sqrt{2}$, where β is an empirical constant of 1.7×10^{-3} , and ΔM is the standard deviation of the

shelf water column weight (kg m^{-2}). For the fjord length and stratification used in our ROMS runs, this expression would give $\bar{v}_F = 0.06 \text{ m s}^{-1}$ for a forcing amplitude of $\eta_S = 20 \text{ m}$ at any forcing frequency and with any fjord width. This value can be compared to \bar{v}_F from ROMS between 0.04 and 0.5 m s^{-1} , which varies with W/R_d and $\omega L/c$ as predicted by the KW model (e.g., Fig. 8). In the Aure model, the fjord response is only a function of the forcing amplitude (sublinearly) and does not depend on fjord width or forcing frequency. Our results show a

linear response with forcing amplitude and a strong dependence on width and forcing frequency, suggesting that the Aure model might not be applicable beyond the fjords for which the empirical relationship was derived.

Our results can also be compared to the slab model of Arneborg (2004), which has recently been used in a modeling study of a Greenlandic fjord (Cowton et al. 2016). For a rectangular fjord with sinusoidal forcing, the slab model in Eq. (2) would predict a velocity amplitude at the mouth of

$$\bar{v}_F = \frac{L}{h_1} \omega \eta_S. \quad (34)$$

This is the same result as the 2D standing wave model in the limit of small $\omega L/c$ [Eq. (11)].

In this slab model, the velocity is linear with forcing frequency (and has no dependence on the fjord width). Cowton et al. (2016) compared a numerical model of Kangderluggsaq Fjord, East Greenland, with the predictions from the slab model and found that the fjord exchange is less sensitive to forcing period than the slab model suggests. Our results could shed some light on this discrepancy. In the KW model [Eq. (22)], fjord velocity scales with frequency as $\bar{v}_F \sim \sin(\omega L/c)$. In the limit of small $\omega L/c$, velocity will scale linearly with ω , as in the slab model. However, as $\omega L/c$ approaches $\pi/2$, the response will be sublinear with ω , perhaps explaining the sublinear relationship in Cowton et al. (2016), where a fjord with $\omega L/c \sim 1$ was modeled.

c. Net exchange and fjord renewal

This study is a step toward understanding the impact of shelf forcing on fjords, but we have not directly addressed the question of net exchange or renewal rates from these flows. Instead, we have described the velocity and density response in the fjord, providing a dynamical framework for understanding these shelf-forced flows. This is a basic step that needs to be addressed before answering questions about the impacts on renewal, heat transport, and other tracer transport (e.g., Gladish and Holland 2015; Sciascia et al. 2014; Cowton et al. 2016; Carroll et al. 2017).

Our results for the excursion length scale indicate that shelf forcing should have increasing impact on fjord renewal and tracer transport for narrow fjords and lower frequencies (Fig. 8). Analogous to the tidal excursion, oscillatory shelf forcing with larger excursions are likely to result in higher dispersion rates than those with shorter excursions. Dispersion from an oscillatory flow field has been studied extensively for tides in typical estuaries (e.g., Fischer 1976; Geyer and Signell 1992;

MacCready and Geyer 2010). Tidal dispersion can result in significant downgradient salt fluxes in some estuaries but only limited fluxes in others. Similarly, there is evidence from the observations in Sermilik that the shelf forcing is important for exporting glacially modified water and renewing the Atlantic water layer (Jackson and Straneo 2016; Jackson et al. 2014).

In the future, these results could be further explored with studies of tracer transport in more realistic model configurations (e.g., Cowton et al. 2016) to quantitatively assess the flushing of the fjord and the spatial patterns of renewal. However, studying tracer transport in the ROMS model of this study is unlikely to yield additional insight into shelf forcing, owing to the idealized geometry of the model—realistic topography is an important component of modeling the tracer dispersion rate in a fjord.

Another simpler approach from the literature is to relate the oscillatory volume flux to an exchange rate by assuming some efficiency ε . For example, Arneborg (2004) finds a 64% efficiency in Gullmar fjord by comparing the velocity field with the time rate of change in various tracers. However, this efficiency could vary significantly in different fjords, not to mention within a particular fjord, so we do not apply this calculation to our volume fluxes. We expect that the exchange efficiency ε varies with geometry/bathymetry, alongshore flow on the shelf, fjord width, and other factors. Within the fjord, the waters near the mouth and in the upper layer (where velocities are larger) should be flushed most rapidly. Toward the head of the fjord, where velocities approach zero, the net exchange from shelf forcing should become negligible. Thus, in the near-glacier region, the buoyancy-driven circulation from a glacier is more likely to dominate the exchange.

d. Limitations of idealized modeling

The modeling of this study is meant to capture the leading-order dynamics of shelf forcing in fjords. There are several aspects of the idealized setup that might warrant further attention in future studies. First, we find that, in our ROMS simulations, the shelf Kelvin waves turn into the fjord and reflect at the head of the fjord with very little dissipation or distortion. Our model contains a flat bottom, vertical walls, and uniform initial stratification, so the waveguide does not vary over the domain and there is only weak dissipation. In reality, the slope Burger number could change along the coast, altering the nature of coastal trapped wave propagation. In particular, the stratification might be significantly different at the head of a fjord where glacial meltwater and discharge enter the fjord at depth. Additionally, bottom friction in a realistic fjord or the presence of

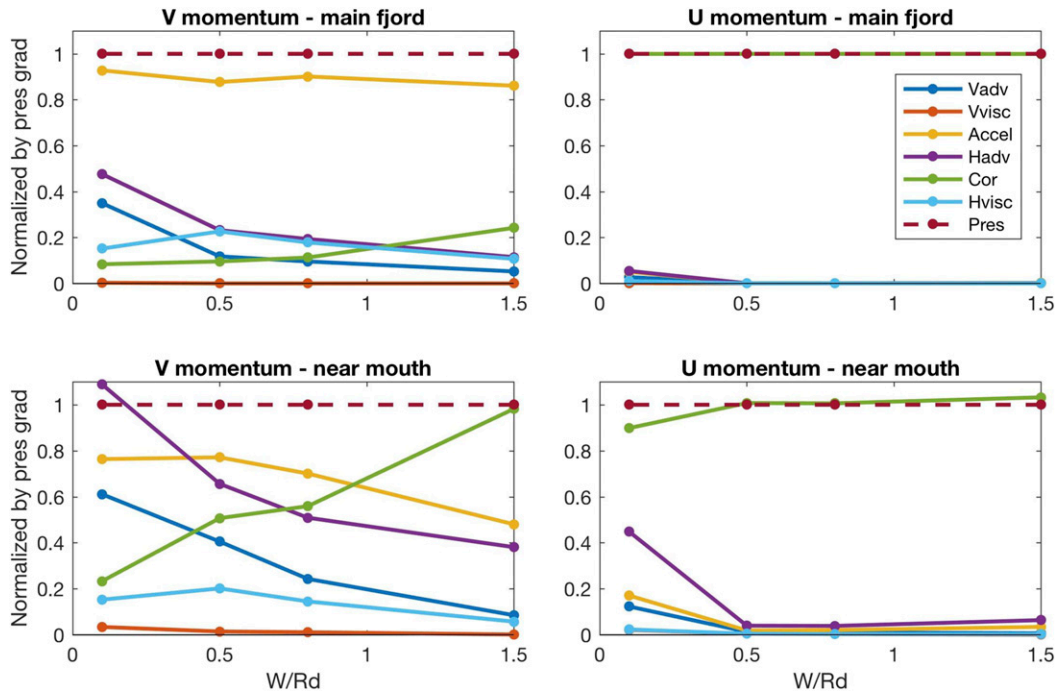


FIG. A1. Momentum budgets for the fjord's upper layer as a function of W/R_d , with the forcing period held constant at 6 days. (left) Along-fjord momentum V . (right) Cross-fjord momentum U . These are spatial averages of the temporal average of the absolute value of each term in the momentum budget. (top) The spatial average over the upper layer of the fjord except the 15 km closest to the mouth. (bottom) The spatial average within 15 km of the fjord mouth. The terms in the momentum budget are vertical advection (Vadv), vertical viscosity (Vvisc), local acceleration (Accel), horizontal advection (Hadv), Coriolis (Cor), Horizontal viscosity (Hvisc), and pressure gradient (Pres). All terms are normalized by the pressure gradient term.

an ice mélange could further alter the propagation of Kelvin waves (MacAyeal et al. 2012).

Our comparison between observations, theory, and ROMS suggests that friction does not play a dominant role in the shelf-forced dynamics of Sermilik Fjord. However, according to Proehl and Rattray (1984), most of the Kelvin wave energy that enters the Strait of Juan de Fuca is dissipated within the fjord. Similarly, Fraser and Inall (2018) find that, in their numerical model of Kangerdlugssuaq Fjord, Greenland, incoming waves are dissipated at the head of the fjord. Thus, the role of dissipation across different fjord systems remains an open question.

Nonlinear effects have only been cursorily addressed here. We show that, for the forcing amplitudes of interest ($\eta_S/h_1 < 0.2$), the fjord response scales linearly with the shelf forcing (Fig. 11c), but the fjord response becomes weakly nonlinear around $\eta_S/h_1 = 0.2$. Future runs with larger-amplitude forcing could be used to test the role of nonlinear effects, perhaps from eddies and jets at the mouth. For all of the simulations except the narrowest fjord forced at resonance, vertical mixing (diagnosed from the k - ϵ mixing scheme within ROMS) is weak and the shape of the pycnocline is effectively unchanged over the simulations. However, mixing might become more

important for larger-amplitude waves or with realistic bathymetry (e.g., as suggested by Fraser and Inall 2018).

Additionally, our model has only considered the dynamics of shelf forcing in isolation. In reality, other modes of circulation—particularly buoyancy forcing and local wind forcing—will interact with the shelf forcing. In summer when freshwater forcing peaks, a mean exchange flow has been observed in Sermilik (Jackson and Straneo 2016). To first order, the shelf-forced dynamics appear the same throughout the year, although the forcing amplitude is reduced in summer. Here we have examined shelf forcing in isolation, but there exist possibilities for nonlinear interaction between these different modes of circulation (e.g., Fraser and Inall 2018).

Eventually, it would be desirable to build on this framework by adding some complexity to the model, such as more realistic bathymetry. In particular, a sill of various depths could be added to the fjord to test the effect of a sill on fjord–shelf exchange. While Sermilik and Kangerdlugssuaq Fjords have sills deeper than 500 m, some fjords around Greenland have shallower sills that might play an important role in controlling the along-fjord transport (Gladish and Holland 2015; Carroll et al. 2017). If a sill is sufficiently shallow (or the

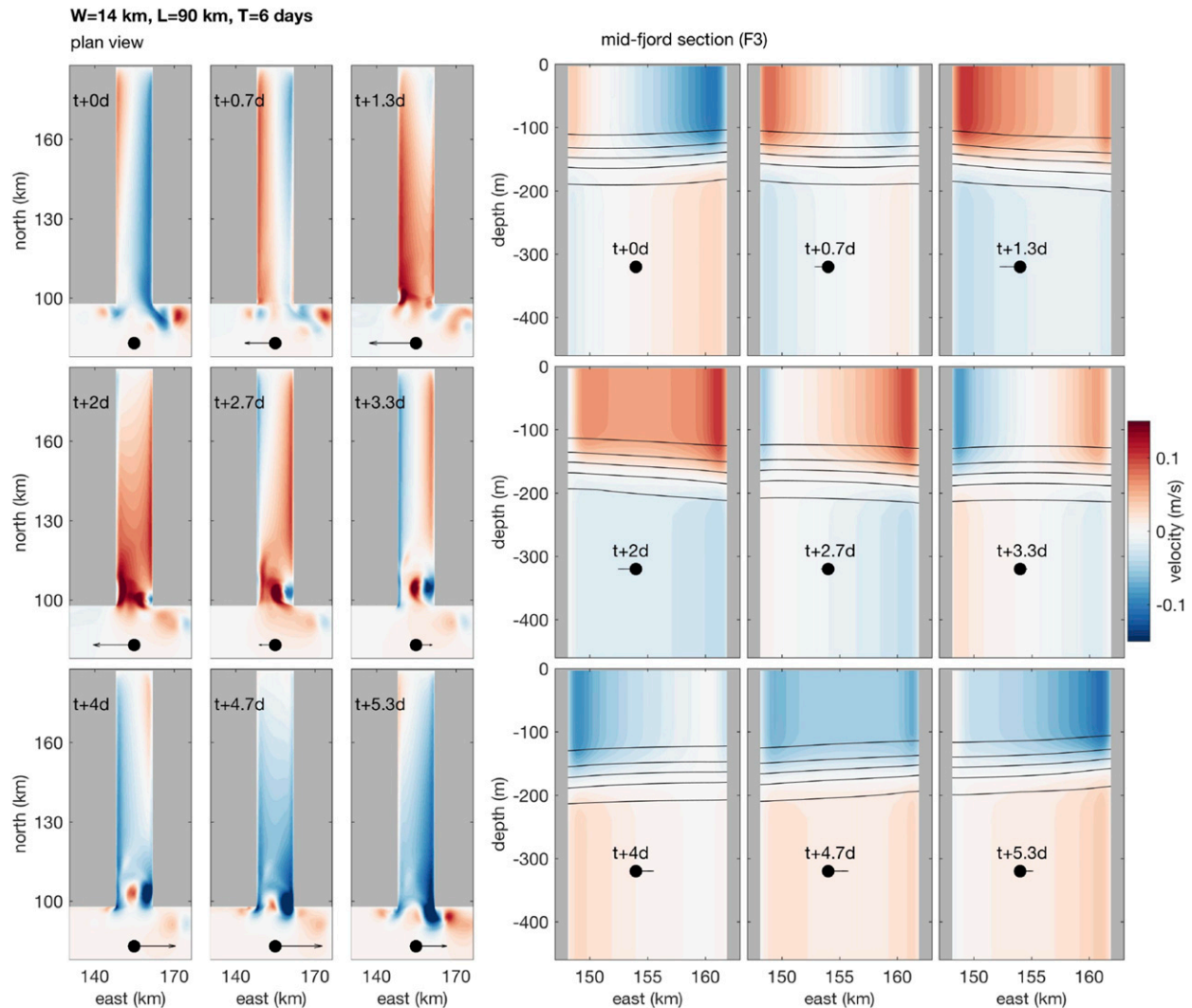


FIG. B1. As in Fig. 7, but for a 14-km-wide fjord ($W/R_d = 1.8$; $\omega L/c = 1$). Along-fjord velocity at nine snapshots over one forcing period. (left) Plan view of northward velocity at 85-m depth, i.e., in the upper layer above the pycnocline. (right) Northward velocity at fjord cross-section F3 at same times as in the left panels. Note: only the upper 450 m is shown, while the full depth is 600 m. In both panels, black arrows show the direction of alongshore shelf wind forcing, and time in days is shown relative to $t = 36$ days from the start of the run. The first five panels have downwelling-favorable winds while the last four have upwelling-favorable winds.

fjord narrow enough), the flow becomes hydraulically controlled, as is the case in many non-Greenlandic fjords (Geyer and Ralston 2011). Additionally, the presence of a sill might alter the stratification, thereby changing the deformation radius and waveguide for Kelvin wave propagation. In the extreme, a sill that is shallower than the pycnocline on the shelf would significantly reduce or eliminate the role of shelf forcing.

5. Conclusions

In this study, we have investigated the role of shelf forcing in driving fjord circulation and transport between a fjord and shelf across a range of fjord geometries

and forcings. In the parameter space of Greenlandic fjords, we find that the fjord response will vary with the fjord width relative to the deformation radius (W/R_d), the along-fjord adjustment time scale relative to the forcing time scale ($\omega L/c$), and the forcing amplitude over the upper-layer thickness (η_S/h_1). A new set of expressions are derived for the velocity, volume flux, and excursion length scale in a fjord, providing a framework for assessing the magnitude of these shelf-forced flows across different fjords. In general, the impact of shelf forcing increases for narrower fjords and lower forcing frequencies (or, equivalently, shorter fjords). We have quantified the bounds where the asymptotic limits of a narrow 2D fjord and very wide fjord (independent sides)

are applicable, and we have explored the transition between these regimes. For fjords with $W/R_d > 0.5$, the fjord response is primarily explained by 3D Kelvin wave dynamics, with a small influence of 2D standing wave dynamics near the resonant forcing frequency. Overall, our results suggest that the cross-shore structure of Kelvin waves should be considered in Greenlandic fjords, contrary to the assumptions in many previous studies. With this improved framework for shelf-forced flows, future studies should further address the net exchange and the flux of heat, salt, and meltwater through Greenland's glacial fjords.

Acknowledgments. This work was funded by NSF Grant OCE-1536856 and by the NOAA Climate and Global Change Postdoctoral Fellowship. We thank Jake Gebbie for providing computing resources and Deepak Cherian for technical help with ROMS and for many valuable discussions about this work. We also thank our two reviewers, John Klinck and Mark Inall, for their constructive and thoughtful comments.

APPENDIX A

Momentum Balances

The fjord's momentum budget is evaluated for the upper layer of the fjord (excluding the mouth region within 15 km of the shelf) as a function of fjord width in Fig. A1. The cross-fjord momentum is in geostrophic balance across all fjord widths: the Coriolis term equals the pressure gradient term, and the other momentum terms are negligible. The along-fjord momentum budget is nearly a balance between pressure and acceleration for all fjord widths, though advection becomes non-negligible (but still small) in the narrowest fjords.

These momentum balances found in ROMS are consistent with the momentum balances assumed by both analytical models. The 2D standing wave model only considers the along-fjord momentum and assumes it to be a balance of pressure and acceleration. The 3D Kelvin wave model assumes a semigeostrophic balance where along-fjord momentum is a balance of pressure and acceleration, and the cross-fjord momentum is geostrophic. Thus, even for an extremely wide fjord, we do not expect the Coriolis term to become important in the along-fjord momentum because of the fundamental balance of Kelvin waves. This is confirmed by the ROMS momentum budgets. For this reason, the momentum budgets cannot help resolve the transition between 2D and 3D dynamics. The Coriolis term is dominant in the cross-fjord momentum budget for all widths, and the Coriolis

term is never important in the along-fjord momentum budget for any width.

These momentum balances for the main portion of the fjord should hold across subinertial forcing periods but would likely break down for higher-frequency forcing. Additionally, the momentum balances look different near the mouth or the head of the fjord, when the Kelvin waves turn corners or change their orientation (Fig. A1).

APPENDIX B

Velocity for 14-km-Wide Fjord ($W/R_d = 1.8$)

Figure B1 shows the along-fjord velocity for a 14-km-wide fjord with a forcing period of 6 days ($W/R_d = 1.8$ and $\omega L/c = 1.0$). One can see enhanced cross-fjord structure compared to the 7-km-wide fjord in Fig. 7, as the Kelvin wave signal becomes trapped on the sides.

REFERENCES

- Allen, J. S., 1975: Coastal trapped waves in a stratified ocean. *J. Phys. Oceanogr.*, **5**, 300–325, [https://doi.org/10.1175/1520-0485\(1975\)005<0300:CTWIAS>2.0.CO;2](https://doi.org/10.1175/1520-0485(1975)005<0300:CTWIAS>2.0.CO;2).
- Arneborg, L., 2004: Turnover times for the water above sill level in Gullmar Fjord. *Cont. Shelf Res.*, **24**, 443–460, <https://doi.org/10.1016/j.csr.2003.12.005>.
- Aure, J., J. Molvær, and A. Stigebrandt, 1996: Observations of inshore water exchange forced by a fluctuating offshore density field. *Mar. Pollut. Bull.*, **33**, 112–119, [https://doi.org/10.1016/S0025-326X\(97\)00005-2](https://doi.org/10.1016/S0025-326X(97)00005-2).
- Bartholomaeus, T. C., L. Stearns, and D. Sutherland, 2016: Contrasts in the response of adjacent fjords and glaciers to ice-sheet surface melt in West Greenland. *Ann. Glaciol.*, **57**, 25–38, <https://doi.org/10.1017/aog.2016.19>.
- Brink, K., 1991: Coastal-trapped waves and wind-driven currents over the continental shelf. *Annu. Rev. Fluid Mech.*, **23**, 389–412, <https://doi.org/10.1146/annurev.fl.23.010191.002133>.
- Carroll, D., D. A. Sutherland, E. L. Shroyer, J. D. Nash, G. A. Catania, and L. A. Stearns, 2017: Subglacial discharge-driven renewal of tidewater glacier fjords. *J. Geophys. Res. Oceans*, **122**, 6611–6629, <https://doi.org/10.1002/2017JC012962>.
- Chauché, N., and Coauthors, 2014: Ice–ocean interaction and calving front morphology at two West Greenland tidewater outlet glaciers. *Cryosphere*, **8**, 1457–1468, <https://doi.org/10.5194/tc-8-1457-2014>.
- Cowton, T., D. Slater, A. Sole, D. Goldberg, and P. Nienow, 2015: Modeling the impact of glacial runoff on fjord circulation and submarine melt rate using a new subgrid-scale parameterization for glacial plumes. *J. Geophys. Res. Oceans*, **120**, 796–812, <https://doi.org/10.1002/2014JC010324>.
- , A. Sole, P. Nienow, D. Slater, D. Wilton, and E. Hanna, 2016: Controls on the transport of oceanic heat to Kangerdlugssuaq Glacier, East Greenland. *J. Glaciol.*, **62**, 1167–1180, <https://doi.org/10.1017/jog.2016.117>.
- Durland, T. S., and B. Qiu, 2003: Transmission of subinertial Kelvin waves through a strait. *J. Phys. Oceanogr.*, **33**, 1337–1350, [https://doi.org/10.1175/1520-0485\(2003\)033<1337:TOSKWT>2.0.CO;2](https://doi.org/10.1175/1520-0485(2003)033<1337:TOSKWT>2.0.CO;2).

- Farmer, D., and H. Freeland, 1983: The physical oceanography of fjords. *Prog. Oceanogr.*, **12**, 147–219, [https://doi.org/10.1016/0079-6611\(83\)90004-6](https://doi.org/10.1016/0079-6611(83)90004-6).
- Fischer, H. B., 1976: Mixing and dispersion in estuaries. *Annu. Rev. Fluid Mech.*, **8**, 107–133, <https://doi.org/10.1146/annurev.fl.08.010176.000543>.
- Fraser, N. J., and M. E. Inall, 2018: Influence of barrier wind forcing on heat delivery toward the Greenland Ice Sheet. *J. Geophys. Res. Oceans*, **123**, 2513–2538, <https://doi.org/10.1002/2017JC013464>.
- Garvine, R. W., 1985: A simple model of estuarine subtidal fluctuations forced by local and remote wind stress. *J. Geophys. Res.*, **90**, 11 945–11 948, <https://doi.org/10.1029/JC090iC06p11945>.
- Geyer, W. R., and R. P. Signell, 1992: A reassessment of the role of tidal dispersion in estuaries and bays. *Estuaries*, **15**, 97–108, <https://doi.org/10.2307/1352684>.
- , and D. Ralston, 2011: The dynamics of strongly stratified estuaries. *Treatise on Estuarine and Coastal Science*, E. Wolanski and D. McLusky, Eds., Elsevier, 37–52.
- Gill, A. E., 1982: *Atmosphere-Ocean Dynamics*. Academic Press, 662 pp.
- Gladish, C. V., and D. M. Holland, 2015: Oceanic boundary conditions for Jakobshavn Glacier. Part I: Variability and renewal of Ilulissat Icefjord waters, 2001–14. *J. Phys. Oceanogr.*, **45**, 3–32, <https://doi.org/10.1175/JPO-D-14-0044.1>.
- Griffies, S. M., and R. W. Hallberg, 2000: Biharmonic friction with a Smagorinsky-like viscosity for use in large-scale eddy-permitting ocean models. *Mon. Wea. Rev.*, **128**, 2935–2946, [https://doi.org/10.1175/1520-0493\(2000\)128<2935:BFWASL>2.0.CO;2](https://doi.org/10.1175/1520-0493(2000)128<2935:BFWASL>2.0.CO;2).
- Harden, B. E., F. Straneo, and D. Sutherland, 2014: Moored observations of synoptic and seasonal variability in the East Greenland Coastal Current. *J. Geophys. Res. Oceans*, **119**, 8838–8857, <https://doi.org/10.1002/2014JC010134>.
- Holbrook, J. R., C. Cannon, and D. G. Kachel, 1983: Two-year observations of coastal-fjord interactions in the strait of Juan de Fuca. *Coastal Oceanography*, H. Gade, A. Edwards, and H. Svendsen, Eds., Plenum, 411–426.
- Holland, D. M., R. H. Thomas, B. de Young, M. H. Ribergaard, and B. Lyberth, 2008: Acceleration of Jakobshavn Isbræ triggered by warm subsurface ocean waters. *Nat. Geosci.*, **1**, 659–664, <https://doi.org/10.1038/ngeo316>.
- Huthnance, J. M., 1978: On coastal trapped waves: Analysis and numerical calculation by inverse iteration. *J. Phys. Oceanogr.*, **8**, 74–92, [https://doi.org/10.1175/1520-0485\(1978\)008<0074:OCTWAA>2.0.CO;2](https://doi.org/10.1175/1520-0485(1978)008<0074:OCTWAA>2.0.CO;2).
- Inall, M. E., and P. A. Gillibrand, 2010: The physics of mid-latitude fjords: A review. *Geol. Soc. London Spec. Publ.*, **344**, 17–33, <https://doi.org/10.1144/SP344.3>.
- , T. Murray, F. R. Cottier, K. Scharrer, T. J. Boyd, K. J. Heywood, and S. L. Bevan, 2014: Oceanic heat delivery via Kangerdlugssuaq Fjord to the south-east Greenland ice sheet. *J. Geophys. Res. Oceans*, **119**, 631–645, <https://doi.org/10.1002/2013JC009295>.
- , F. Nilsen, F. R. Cottier, and R. Daae, 2015: Shelf/fjord exchange driven by coastal-trapped waves in the Arctic. *J. Geophys. Res. Oceans*, **120**, 8283–8303, <https://doi.org/10.1002/2015JC011277>.
- Jackson, R. H., and F. Straneo, 2016: Heat, salt, and freshwater budgets for a glacial fjord in Greenland. *J. Phys. Oceanogr.*, **46**, 2735–2768, <https://doi.org/10.1175/JPO-D-15-0134.1>.
- , —, and D. A. Sutherland, 2014: Externally forced fluctuations in ocean temperature at Greenland glaciers in non-summer months. *Nat. Geosci.*, **7**, 503–508, <https://doi.org/10.1038/ngeo2186>.
- Janzen, C. D., and K. C. Wong, 2002: Wind-forced dynamics at the estuary-shelf interface of a large coastal plain estuary. *J. Geophys. Res.*, **107**, 3138, <https://doi.org/10.1029/2001JC000959>.
- Jenkins, A., 2011: Convection-driven melting near the grounding lines of ice shelves and tidewater glaciers. *J. Phys. Oceanogr.*, **41**, 2279–2294, <https://doi.org/10.1175/JPO-D-11-03.1>.
- Johnson, H. L., and C. Garrett, 2006: What fraction of a Kelvin wave incident on a narrow strait is transmitted? *J. Phys. Oceanogr.*, **36**, 945–954, <https://doi.org/10.1175/JPO2896.1>.
- , A. Münchow, K. K. Falkner, and H. Melling, 2011: Ocean circulation and properties in Petermann Fjord, Greenland. *J. Geophys. Res.*, **116**, C01003, <https://doi.org/10.1029/2010JC006519>.
- Joughin, I., R. B. Alley, and D. M. Holland, 2012: Ice-sheet response to oceanic forcing. *Science*, **338**, 1172–1176, <https://doi.org/10.1126/science.1226481>.
- Kantha, L. H., and C. A. Clayson, 1994: An improved mixed layer model for geophysical applications. *J. Geophys. Res.*, **99**, 25 235–25 266, <https://doi.org/10.1029/94JC02257>.
- Klinck, J., J. O'Brien, and H. Svendsen, 1981: Simple model of fjord and coastal circulation interaction. *J. Phys. Oceanogr.*, **11**, 1612–1626, [https://doi.org/10.1175/1520-0485\(1981\)011<1612:ASMOFA>2.0.CO;2](https://doi.org/10.1175/1520-0485(1981)011<1612:ASMOFA>2.0.CO;2).
- MacAyeal, D. R., J. Freed-Brown, W. W. Zhang, and J. M. Amundson, 2012: The influence of ice mélange on fjord seiches. *Ann. Glaciol.*, **53**, 45–49, <https://doi.org/10.3189/2012/AoG60A027>.
- MacCready, P., and W. R. Geyer, 2010: Advances in estuarine physics. *Annu. Rev. Mar. Sci.*, **2**, 35–58, <https://doi.org/10.1146/annurev-marine-120308-081015>.
- Mason, E., J. Molemaker, A. F. Shchepetkin, F. Colas, J. C. McWilliams, and P. Sangrà, 2010: Procedures for offline grid nesting in regional ocean models. *Ocean Modell.*, **35**, 1–15, <https://doi.org/10.1016/j.ocemod.2010.05.007>.
- Moore, G., and I. Renfrew, 2005: Tip jets and barrier winds: A QuikSCAT climatology of high wind speed events around Greenland. *J. Climate*, **18**, 3713–3725, <https://doi.org/10.1175/JCLI3455.1>.
- Mortensen, J., K. Lennert, J. Bendtsen, and S. Rysgaard, 2011: Heat sources for glacial melt in a sub-Arctic fjord (Godthåbsfjord) in contact with the Greenland Ice Sheet. *J. Geophys. Res.*, **116**, C01013, <https://doi.org/10.1029/2010JC006528>.
- Nick, F. M., A. Vieli, I. M. Howat, and I. Joughin, 2009: Large-scale changes in Greenland outlet glacier dynamics triggered at the terminus. *Nat. Geosci.*, **2**, 110–114, <https://doi.org/10.1038/ngeo394>.
- Oltmanns, M., F. Straneo, G. W. K. Moore, and S. H. Mernild, 2014: Strong downslope wind events in Ammassalik, southeast Greenland. *J. Climate*, **27**, 977–993, <https://doi.org/10.1175/JCLI-D-13-00067.1>.
- Pettersson, H., 1920: Internal movements in coastal waters and meteorological phenomena. *Geogr. Ann. Stockholm*, **1**, 32–66.
- Proehl, J. A., and M. Rattray, 1984: Low-frequency response of wide deep estuaries to non-local atmospheric forcing. *J. Phys. Oceanogr.*, **14**, 904–921, [https://doi.org/10.1175/1520-0485\(1984\)014<0904:LFROWD>2.0.CO;2](https://doi.org/10.1175/1520-0485(1984)014<0904:LFROWD>2.0.CO;2).
- Sciascia, R., C. Cenedese, D. Nicoli, P. Heimbach, and F. Straneo, 2014: Impact of periodic intermediary flows on submarine melting of a Greenland glacier. *J. Geophys. Res. Oceans*, **119**, 7078–7098, <https://doi.org/10.1002/2014JC009953>.
- Shchepetkin, A. F., and J. C. McWilliams, 2005: The Regional Oceanic Modeling System (ROMS): A split-explicit, free-surface,

- topography-following-coordinate oceanic model. *Ocean Modell.*, **9**, 347–404, <https://doi.org/10.1016/j.ocemod.2004.08.002>.
- Spall, M. A., R. H. Jackson, and F. Straneo, 2017: Katabatic wind-driven exchange in fjords. *J. Geophys. Res. Oceans*, **122**, 8246–8262, <https://doi.org/10.1002/2017JC013026>.
- Stigebrandt, A., 1981: A mechanism governing the estuarine circulation in deep, strongly stratified fjords. *Estuarine Coastal Shelf Sci.*, **13**, 197–211, [https://doi.org/10.1016/S0302-3524\(81\)80076-X](https://doi.org/10.1016/S0302-3524(81)80076-X).
- , 1990: On the response of the horizontal mean vertical density distribution in a fjord to low-frequency density fluctuations in the coastal water. *Tellus*, **42**, 605–614, <https://doi.org/10.3402/tellusa.v42i5.11902>.
- , 2010: Fjord circulation. *Encyclopedia of Ocean Sciences*, J. Steele, S. Thorpe, and K. Turekian, Eds., Elsevier, 353–358.
- , 2012: Hydrodynamics and circulation of fjords. *Encyclopedia of Lakes and Reservoirs*, L. Bengtsson, R. W. Herschy, and R. W. Fairbridge, Eds., Springer Science, 327–344.
- , and J. Aure, 1990: The importance of external driving forces for the water exchange in the fjords from Skagerrak to Finnmark. Institute of Marine Research Rep. FO9003, 29 pp.
- Straneo, F., and P. Heimbach, 2013: North Atlantic warming and the retreat of Greenland's outlet glaciers. *Nat. Commun.*, **504**, 36–43, <https://doi.org/10.1038/nature12854>.
- , and C. Cenedese, 2015: The dynamics of Greenland's glacial fjords and their role in climate. *Ann. Rev. Mar. Sci.*, **7**, 89–112, <https://doi.org/10.1146/annurev-marine-010213-135133>.
- , G. S. Hamilton, D. A. Sutherland, L. A. Stearns, F. Davidson, M. O. Hammill, G. B. Stenson, and A. Rosing-Asvid, 2010: Rapid circulation of warm subtropical waters in a major glacial fjord in East Greenland. *Nat. Geosci.*, **3**, 182–186, <https://doi.org/10.1038/ngeo764>.
- , R. G. Curry, D. A. Sutherland, G. S. Hamilton, C. Cenedese, K. Våge, and L. A. Stearns, 2011: Impact of fjord dynamics and glacial runoff on the circulation near Helheim Glacier. *Nat. Geosci.*, **4**, 322–327, <https://doi.org/10.1038/ngeo1109>.
- Sutherland, D. A., F. Straneo, and R. S. Pickart, 2014: Characteristics and dynamics of two major Greenland glacial fjords. *J. Geophys. Res. Oceans*, **119**, 3767–3791, <https://doi.org/10.1002/2013JC009786>.
- Svendsen, H., 1980: Exchange processes above sill level between fjords and coastal water. *Fjord Oceanography*, H. Freeland, D. Farmer, and C. D. Levings, Eds., Plenum Press, 355–362.
- Taylor, G. I., 1921: Tidal oscillations in gulfs and rectangular basins. *Proc. London Math. Soc.*, **20**, 148–181.
- Toulany, B., and C. Garrett, 1984: Geostrophic control of fluctuating barotropic flow through straits. *J. Phys. Oceanogr.*, **14**, 649–655, [https://doi.org/10.1175/1520-0485\(1984\)014<0649:GCOFBF>2.0.CO;2](https://doi.org/10.1175/1520-0485(1984)014<0649:GCOFBF>2.0.CO;2).
- Wang, D.-P., 1979: Wind-driven circulation in the Chesapeake Bay, winter 1975. *J. Phys. Oceanogr.*, **9**, 564–572, [https://doi.org/10.1175/1520-0485\(1979\)009<0564:WDCITC>2.0.CO;2](https://doi.org/10.1175/1520-0485(1979)009<0564:WDCITC>2.0.CO;2).
- Warner, J. C., C. R. Sherwood, H. G. Arango, and R. P. Signell, 2005: Performance of four turbulence closure models implemented using a generic length scale method. *Ocean Modell.*, **8**, 81–113, <https://doi.org/10.1016/j.ocemod.2003.12.003>.
- Xu, Y., E. Rignot, D. Menemenlis, and M. Koppes, 2012: Numerical experiments on subaqueous melting of Greenland tidewater glaciers in response to ocean warming and enhanced subglacial discharge. *Ann. Glaciol.*, **53**, 229–234, <https://doi.org/10.3189/2012AoG60A139>.